



HAL
open science

Comparative study of Yb:Lu₃Al₅O₁₂ and Yb:Lu₂O₃ laser ceramics produced from laser-ablated nanopowders

Liza Basyrova, Pavel Loiko, Roman Maksimov, Vladislav Shitov, Josep Maria Serres, Uwe Griebner, Valentin Petrov, Magdalena Aguiló, Francesc Díaz, Xavier Mateos

► To cite this version:

Liza Basyrova, Pavel Loiko, Roman Maksimov, Vladislav Shitov, Josep Maria Serres, et al.. Comparative study of Yb:Lu₃Al₅O₁₂ and Yb:Lu₂O₃ laser ceramics produced from laser-ablated nanopowders. *Ceramics International*, 2021, 47 (5), pp.6633-6642. 10.1016/j.ceramint.2020.10.253 . hal-03368757

HAL Id: hal-03368757

<https://hal.science/hal-03368757v1>

Submitted on 7 Oct 2021

HAL is a multi-disciplinary open access archive for the deposit and dissemination of scientific research documents, whether they are published or not. The documents may come from teaching and research institutions in France or abroad, or from public or private research centers.

L'archive ouverte pluridisciplinaire **HAL**, est destinée au dépôt et à la diffusion de documents scientifiques de niveau recherche, publiés ou non, émanant des établissements d'enseignement et de recherche français ou étrangers, des laboratoires publics ou privés.

Comparative study of Yb:Lu₃Al₅O₁₂ and Yb:Lu₂O₃ laser ceramics produced from laser-ablated nanopowders

Liza Basyrova,^{1,2} Pavel Loiko,³ Roman Maksimov,^{4,5} Vladislav Shitov,⁵ Josep Maria Serres,¹ Uwe Griebner,⁶ Valentin Petrov,⁶ Magdalena Aguiló,¹ Francesc Díaz,¹ and Xavier Mateos^{1,*}

¹*Universitat Rovira i Virgili (URV), Física i Cristal·lografia de Materials i Nanomaterials (FiCMA-FiCNA), Marcel·li Domingo 1, 43007 Tarragona, Spain*

²*ITMO University, 49 Kronverkskiy Pr., 197101 Saint-Petersburg, Russia*

³*Centre de Recherche sur les Ions, les Matériaux et la Photonique (CIMAP), UMR 6252 CEA-CNRS-ENSICAEN, Université de Caen Normandie, 6 Boulevard du Maréchal Juin, 14050 Caen Cedex 4, France*

⁴*Ural Federal University, 19 Mira St., 620002 Ekaterinburg, Russia*

⁵*Institute of Electrophysics, Ural Branch of the Russian Academy of Sciences, 106 Amundsen St., 620016 Ekaterinburg, Russia*

⁶*Max Born Institute for Nonlinear Optics and Short Pulse Spectroscopy, Max-Born-Str. 2a, 12489 Berlin, Germany*

*Corresponding author, e-mail: xavier.mateos@urv.cat

Abstract: We present a comparative study of two Lu-based oxide ceramics doped with Yb³⁺ ions, namely Yb:Lu₃Al₅O₁₂ (garnet) and Yb:Lu₂O₃ (sesquioxide), promising for thin-disk lasers. The ceramics are fabricated using nanopowders of 3.6 at.% Yb:Lu₂O₃ and Al₂O₃ produced by laser ablation: Yb:Lu₃Al₅O₁₂ – by vacuum sintering at 1800 °C for 5 h with the addition of 1 wt% TEOS as a sintering aid, and Yb:Lu₂O₃ – by vacuum pre-sintering at 1250 °C for 2 h followed by Hot Isostatic Pressing at 1400 °C for 2 h under Ar gas pressure of 207 MPa. The comparison includes the structure, Raman spectra, transmission, optical spectroscopy and laser operation. The crystal-field splitting of Yb³⁺ multiplets is revealed for Lu₃Al₅O₁₂. A continuous-wave (CW) Yb:Lu₃Al₅O₁₂ ceramic microchip laser generates 5.65 W at 1031.1 nm with a slope efficiency of 67.2%. In the quasi-CW regime, the peak power is scaled up to 8.83 W. The power scaling for the Yb:Lu₂O₃ ceramic laser is limited by losses originating from residual coloration and inferior thermal behavior.

Keywords: garnets; sesquioxides; optical ceramics; laser operation.

1. Introduction

Transparent ceramics are fully dense single-phase polycrystalline materials containing μm -sized grains and featuring high light transmission in a broad spectral range [1,2]. High transmission is ensured by: (i) very small porosity, (ii) absence of a second phase at the grain boundaries – negligible difference of the optical properties between the grains and their boundaries, (iii) high quality grain boundaries, (iv) small grain size with narrow and spatially uniform size distribution, (v) isotropic lattice structure and (vi) high surface quality. Under such conditions, transparent ceramics are of interest for fabrication of photonic elements.

Recently, transparent ceramics doped with rare-earth ions (RE^{3+}) such as Nd^{3+} [3,4], Yb^{3+} [5,6], Tm^{3+} [7], Ho^{3+} [8], *etc.*, have attracted research interest for implementation in near-infrared lasers. As defined by the condition of isotropic structure, cubic materials mainly belonging to two crystal families were employed for this aim, namely, garnets $\text{RE}_3\text{Al}_5\text{O}_{12}$ ($\text{RE} = \text{Y}, \text{Lu}$) [9,10] and sesquioxides A_2O_3 ($\text{A} = \text{Y}, \text{Lu}, \text{Sc}$ or their mixture) [11-13]. Transparent laser ceramics offer several advantages as compared to the corresponding single-crystals, i.e., (i) easier fabrication method, (ii) lower synthesis temperature (cf. the high-melting temperature sesquioxides [11,12]); (iii) higher RE^{3+} doping levels [5,14], (iv) size-scalable production and (v) possibility to fabricate compositionally “mixed” structures [13,15].

The first studies on laser ceramics focused on Nd^{3+} doping for laser emission at $\sim 1.06 \mu\text{m}$ [3,4]. Later on, the interest shifted to the ytterbium (Yb^{3+}) ion [5,6]. Yb^{3+} provides broader emission bandwidth around $\sim 1 \mu\text{m}$ allowing for wavelength tuning and generation of ultrashort pulses. The simple energy-level scheme eliminates energy-transfer upconversion. Yb^{3+} -doped materials can be efficiently pumped by commercial and high-power InGaAs laser diodes at 930-980 nm leading to high Stokes efficiency and much weaker heat loading (as compared to the Nd^{3+} -doped ones). Yb^{3+} -doped laser ceramics are thus important for applications in power-scalable continuous-wave (CW) [5,16,17] and mode-locked bulk [18,19] and thin-disk [20] lasers at $\sim 1 \mu\text{m}$.

It was shown that Lu-based oxides (e.g., $\text{Lu}_3\text{Al}_5\text{O}_{12}$ and Lu_2O_3 [10]) are more suitable for Yb^{3+} doping as compared to their Y-counterparts [21,22]. This is because of the relatively small difference of ionic radii between Yb^{3+} and Lu^{3+} which leads to weaker lattice distortions, lower scattering losses, easier doping with close to 100% segregation coefficient and better thermal properties. Lu-based oxides show much weaker dependences of thermal conductivity κ on the Yb doping level and the temperature (as compared to Y-oxides) whilst the κ values of undoped materials are close. The thermal conductivity of $\text{Yb}:\text{Lu}_3\text{Al}_5\text{O}_{12}$ ($\kappa \sim 7.5 \text{ Wm}^{-1}\text{K}^{-1}$ for few at.% Yb doping at room temperature) already becomes superior to that of $\text{Yb}:\text{Y}_3\text{Al}_5\text{O}_{12}$ at relatively low doping levels [21]. This has a direct influence on the power scaling capabilities of lasers [10].

Transparent $\text{Yb}:\text{Lu}_3\text{Al}_5\text{O}_{12}$ ceramics have been fabricated by different methods and their diode-pumped laser performance has been already studied [6,17,18,22,23]. It was shown that $\text{Yb}:\text{Lu}_3\text{Al}_5\text{O}_{12}$ ceramic lasers outperform those based on single-crystals [24]. Fu *et al.* reported on 2.5 at.% $\text{Yb}:\text{Lu}_3\text{Al}_5\text{O}_{12}$ ceramics fabricated by solid-state sintering at 1850 °C for 50 h using commercial powders generating 2.1 W at 1030 nm with a slope efficiency of

41.7% [22]. Pirri *et al.* demonstrated a highly-doped 10 at.% Yb:Lu₃Al₅O₁₂ ceramic laser diode-pumped at 936 nm delivering 6.0 W at 1030 nm with a slightly higher slope efficiency of 52% [25]. Yb:Lu₃Al₅O₁₂ ceramic thin-disk lasers are also known: Nakao *et al.* developed such a thin-disk laser with an output power of 166 W and a slope efficiency of 72.2% [10].

Recently, we proposed a novel approach to fabricate transparent Yb:Lu₃Al₅O₁₂ ceramics by using laser-ablated Yb:Lu₂O₃ and Al₂O₃ nanopowders and tetraethoxysilane (TEOS) as a sintering additive [26]. It allowed us to reduce the synthesis temperature down to 1800 °C while maintaining the good optical quality of the ceramics.

In the present work, we report on efficient and power-scalable diode-pumped operation of transparent Yb:Lu₃Al₅O₁₂ ceramics fabricated using laser-ablated nanoparticles by employing a compact (microchip-type) laser design. For comparison, we also studied Yb:Lu₂O₃ ceramics produced from the corresponding laser-ablated nanopowder. The structural, optical and spectroscopic properties of the two ceramics are compared.

2. Synthesis of ceramics

For the fabrication of the Yb³⁺-doped ceramics, we used Yb:Lu₂O₃ and Al₂O₃ nanopowders (mean particle size: 34 nm and 29 nm, respectively) synthesized by laser ablation and subsequent sedimentation [26,27]. This approach allowed us to produce nanopowders with a narrow particle size distribution which has a positive effect on the transparency of ceramics.

To fabricate Yb:Lu₃Al₅O₁₂ garnet ceramics, both nanopowders were used. To achieve a stoichiometric Al/(Yb + Lu) ratio corresponding to (Yb_{0.036}Lu_{0.964})₃Al₅O₁₂ composition, the nanopowders were converted into the cubic phase by calcining at 900–1200 °C for 3 hours (h) in air. The calcined powders were weighed and mixed by ball milling in ethyl alcohol for 48 h with an addition of 1 wt% of TEOS (Si(OC₂H₅)₄) as a sintering aid. After drying, the mixture was compacted into a cylindrical pellet by uniaxial static pressing at 200 MPa. The obtained compact powder was sintered at 1800 °C for 5 h in a vacuum furnace with graphite heaters at a residual gas pressure of 10⁻³ Pa. The as-sintered blue-colored ceramic disk (diameter: $\Phi = 14$ mm, thickness: $t = 2$ mm) was annealed in air at 1300 °C for 5 h to remove the coloration originating from oxygen vacancies and Yb²⁺ species appearing in oxygen-deficient atmosphere [26,28]. As a result, a transparent and colorless sample was obtained, Fig. 1.

The formation of SiO₂-rich liquid phase during sintering of Yb:Lu₃Al₅O₁₂ ceramics with the addition of TEOS promotes mass transfer and densification enabling almost pore-free microstructure using conventional vacuum sintering. However, the complete elimination of pores in sesquioxides is difficult because the conventional sintering usually requires high temperatures for full densification, which often results in grain-entrapped pores due to a rapid grain growth at the final stage of sintering. One of the approaches to avoid the breakaway of pores from the grain boundaries is based on the reduction of the sintering temperature by using pressure-assisted densification methods such as Hot Isostatic Pressing (HIP). Consequently, to fabricate the Yb:Lu₂O₃ ceramics, the laser-ablated Yb:Lu₂O₃ nanopowder was compacted by uniaxial dry-pressing at 200 MPa and then pre-sintered under vacuum at

1250 °C for 2 h. The pre-sintered sample was subjected to a capsule-free post-HIP step under an Ar gas pressure of 207 MPa at a temperature of 1400 °C for 2 h.

The obtained Yb:Lu₂O₃ ceramic disk with dimensions similar to those for Yb:Lu₃Al₅O₁₂ was transparent but had a deep-brown coloration. The latter is assigned to oxygen vacancies forming during HIP in the oven with graphite heaters (forming reducer conditions). To remove the coloration, the ceramic was annealed in air. We studied the effect of annealing temperature and duration on the sample transmission, Fig. 2. For this, we used a similar Yb:Lu₂O₃ sample obtained by vacuum pre-sintering at 1400 °C for 1 h followed by HIP at 1500 °C for 2 h. For the annealing temperature of 1200 °C with increasing the treatment time from 1 to 10 h, the in-line transmission of the ceramic disk T_0 gradually increases from 75.5% to 77.7% (at the wavelength of 1.10 μm) which is well above the transmission for the as-HIPed ceramics ($T_0 = 71.1%$). Further increase of this time above 10 h does not improve the sample transmission. However, the annealing at 1300 °C for 1 h results in a notable drop of T_0 . A similar effect was observed previously in [29] and was assigned to the intense growth of nm-sized pores at ambient pressure and temperature high enough to activate the solid-phase processes. Thus, the sample used for the laser studies was annealed at 1200 °C for 10 h in air, see Fig. 1. It maintained a weak grey-brown coloration.

The drop in the transmission in the visible spectral range for annealed Yb:Lu₂O₃ ceramics (and, respectively, its residual coloration) may be explained as follows. First, it can originate from the presence of sub-μm and nm sized pores. According to the Rayleigh law, the scattering intensity is proportional to the squared volume of the defect and inverse proportional to λ^4 . Considering that the content of scattering centers detected using optical microscopy is relatively low (see Section 2.2), we conclude that the scattering centers with characteristic diameter above 2 μm cannot be responsible for the considerable decrease in light transmission at short wavelengths. Second, the coloration can be caused by impurity ions. We analyzed the impurity composition of the Yb:Lu₂O₃ ceramic by Inductively Coupled Plasma Mass Spectrometry (ICP-MS) indicating the following uncontrolled impurities: transition-metal elements – Mn and Ti (both ~12 ppm) and rare-earth ones – Gd and Tb (both ~10 ppm) and Ho (7 ppm). Further discussion of the evidence for the presence of Tb³⁺ species in the ceramics is presented in Section 3.2.

The doping level for both ceramics is the same, 3.6±0.4 at.%, determined by the composition of the Yb:Lu₂O₃ nanoparticles analyzed using ICP-MS, while the ion density N_{Yb} is different, namely $5.1 \times 10^{20} \text{ cm}^{-3}$ for Yb:Lu₃Al₅O₁₂ (measured density: $\rho = 6.70 \text{ g/cm}^3$) and $10.2 \times 10^{20} \text{ cm}^{-3}$ for Yb:Lu₂O₃ ($\rho = 9.41 \text{ g/cm}^3$).

For the spectroscopic studies, the disks were double-sided polished to laser-grade quality.

3. Experimental

The structure and the phase purity of the two ceramics were studied by X-ray powder diffraction (XRD) analysis using a Shimadzu XRD-6000 diffractometer and Cu K α radiation with a Ni filter.

The distribution of scattering centers (μm -sized pores) through the depth of the ceramic disks was analyzed by direct counting using an optical microscope (Olympus BX51TRF). The selected disk volume ($577 \times 433 \times 50 \mu\text{m}^3$) was in-depth scanned starting from one sample surface and moving down reaching the opposite surface with a step of $50 \mu\text{m}$ by changing the position of the focus. The spatial resolution of the microscope was $\sim 2 \mu\text{m}$, so that smaller pores than this size were not visualized.

The microstructure of a fractured surface of both ceramics was studied by Scanning Electron Microscopy (SEM) using a MERLIN SEM microscope (Carl Zeiss), Fig. 5. The SEM images were analyzed with the ImageJ software counting >100 grains and a shape factor of 1.2 was applied.

The room temperature (RT, 293 K) in-line transmission spectra of annealed and laser-grade polished ceramic disks were measured using a Shimadzu UV-3600 spectrophotometer. The luminescence spectra were measured with an optical spectrum analyzer (AQ6370B, Yokogawa) using a Ti:Sapphire laser tuned to 976 nm as an excitation source. For the low-temperature (LT, 6 K) absorption and luminescence studies, we used a cryostat (SU 12, Oxford Instruments Ltd.) with helium-gas close-cycle flow.

The luminescence decay curves were measured at RT for powdered samples to avoid the effect of radiation trapping. We used a 1/4 m monochromator (Oriel 77200), an InGaAs detector and an 8 GHz digital oscilloscope (DSA70804B, Tektronix). The luminescence was excited by the output of a ns optical parametric oscillator (Horizon, Continuum) tuned to 970 nm.

The RT Raman spectra were measured with a Renishaw inVia confocal Raman microscope using a $\times 50$ Leica objective (N.A. = 0.75). The excitation was at 488 nm (Ar⁺ ion laser line) and the spectral resolution was $\sim 1 \text{ cm}^{-1}$.

4. Characterization of ceramics

4.1 Structure and microstructure

The X-ray powder diffraction patterns of ceramics are shown in Fig. 3. Both ceramics are of single-phase nature. The Yb:Lu₃Al₅O₁₂ ceramic exhibits a cubic structure identical to that of undoped Lu₃Al₅O₁₂ (International Centre for Diffraction Data, ICDD card #73-1368, sp. gr. $Ia\bar{3}d - O_{10}^h$, No. 230). The lattice constant is $a = 11.912 \text{ \AA}$. The Yb³⁺ ions in Lu₃Al₅O₁₂ replace the host-forming Lu³⁺ cations in a single type of sites (symmetry: D₂, coordination number (C.N.) by oxygen: VIII) and their ionic radii are $R_{\text{Yb}} = 0.985 \text{ \AA}$ and $R_{\text{Lu}} = 0.977 \text{ \AA}$ [30]. This difference determines a slight increase of the lattice parameter a with respect to undoped Lu₃Al₅O₁₂ ($a = 11.90 \text{ \AA}$).

The Yb:Lu₂O₃ ceramic is also cubic (sp. gr. $Ia\bar{3} - T_h^7$, No. 206) and possesses the so-called bixbyite ((Mn,Fe)₂O₃-type) or C-type structure [31] of undoped Lu₂O₃ (ICDD card #76-0162). In the bixbyite structure, there are two crystallographic sites for RE³⁺ ions replacing the Lu³⁺ cations (symmetry: C₂ and C_{3i}, C.N. by oxygen: VI). The optical properties are mainly determined by the majority of ions residing in the C₂ sites (for the C_{3i} site, the electric-dipole transitions are forbidden due to inversion symmetry) [32]. The Yb³⁺ ions in Lu₂O₃ have lower coordination than in garnets (Lu₃Al₅O₁₂) and shorter Yb|Lu – O

interatomic distances leading to a stronger crystal field. The lattice constant for the Yb:Lu₂O₃ ceramics is $a = 10.401 \text{ \AA}$, slightly larger compared to undoped Lu₂O₃ ($a = 10.391 \text{ \AA}$).

The results on the distribution of scattering centers (μm -sized pores) through the depth of the ceramic disks are shown in Fig. 4. The very high content of scattering centers near one of the surfaces is explained by the polishing quality (pre-polish prior to the actual laser-grade-polish). The mean concentration of μm -sized pores X_{pore} is 9.8 ppm for Yb:Lu₃Al₅O₁₂ and 3.5 ppm for Yb:Lu₂O₃ ceramics.

The SEM images of a fractured surface of both ceramics are shown in Fig. 5. The Yb:Lu₃Al₅O₁₂ ceramics exhibited a close-packed microstructure with relatively large grains (mean size: $D_{\text{grain}} = 14 \mu\text{m}$), clean grain boundaries and a very low content of sub- μm sized pores. The grain size distribution was similar over different parts of the ceramic disk. For the Yb:Lu₂O₃ ceramics, much smaller grains were observed with $D_{\text{grain}} = 0.4 \mu\text{m}$. The ceramics also featured a close-packed structure. The difference in the mean grain size is related mainly to the different sintering temperature.

4.2 Optical spectroscopy

The in-line transmission spectra of annealed and laser-grade polished Yb:Lu₃Al₅O₁₂ and Yb:Lu₂O₃ ceramic disks recalculated to the same thickness t of 1.0 mm are shown in Fig. 6. They are compared with the upper limit of transmission set by the Fresnel losses.

For the Yb:Lu₃Al₅O₁₂ ceramic disk at the wavelength of $1.10 \mu\text{m}$ (out of the Yb³⁺ absorption), the measured low-signal transmission was $T_0 = 83.0\%$, which is very close to the theoretical limit, $T_{\text{Fr}} = 83.7\%$ (calculated for a refractive index $n = 1.824$ [33]). The ceramics also exhibited excellent transparency in the visible with the UV absorption edge at $\sim 230 \text{ nm}$. For the Yb:Lu₂O₃ ceramic disk, $T_0 = 81.3\%$ at $1.10 \mu\text{m}$, cf. with $T_{\text{Fr}} = 81.5\%$ corresponding to a refractive index $n = 1.909$ [34]. For this ceramic sample, the absorption in the visible gradually decreased reaching the UV absorption edge at $\sim 270 \text{ nm}$.

The room temperature (RT, 293 K) absorption cross-sections for Yb³⁺ were calculated from the absorption coefficient, $\sigma_{\text{abs}} = \alpha_{\text{abs}}/N_{\text{Yb}}$, where $\alpha_{\text{abs}} = -\ln(T_0/T_{\text{Fr}})/t$. For Yb:Lu₃Al₅O₁₂, at the zero-phonon line (ZPL, i.e., the transition between the lowest Stark sub-levels of Yb³⁺ multiplets), σ_{abs} is $0.63 \times 10^{-20} \text{ cm}^2$ at 968.4 nm , see Fig. 7(a). The full width at half maximum (FWHM) of the absorption peak is 3.9 nm . A broad (FWHM $> 20 \text{ nm}$) and structured absorption band is observed at shorter wavelengths with a maximum at 936.3 nm . For Yb:Lu₂O₃, $\sigma_{\text{abs}} = 1.77 \times 10^{-20} \text{ cm}^2$ for the ZPL at 976.2 nm with a FWHM of 3.3 nm .

The RT stimulated-emission (SE) cross-sections, σ_{SE} , were calculated using the reciprocity method (RM) [35]:

$$\sigma_{\text{SE}}(\lambda) = \sigma_{\text{abs}}(\lambda) \frac{Z_1}{Z_2} \exp\left(-\frac{hc/\lambda - E_{\text{ZPL}}}{kT}\right), \quad (1a)$$

$$Z_m = \sum_k g_k^m \exp(-E_k^m / kT). \quad (1b)$$

Here, h is the Planck constant, c is the speed of light, λ is the light wavelength, k is the Boltzmann constant, T is the crystal temperature, E_{ZPL} is the ZPL energy, and Z_m are the partition functions of the lower ($m = 1$) and the upper ($m = 2$) multiplets, g_k^m (assumed to be

1) is the degeneracy of the sub-level with the number k and the energy E^m_k measured from the lowest sub-level of each multiplet. The Stark splitting for $\text{Yb}^{3+}:\text{Lu}_3\text{Al}_5\text{O}_{12}$ was determined from low-temperature (LT) spectroscopy, and for $\text{Yb}^{3+}:\text{Lu}_2\text{O}_3$ – was taken from [36]. The resulting SE cross-section spectra are shown in Fig. 7(a),(c).

In the long-wavelength part of the SE cross-section spectrum, the application of the RM leads to high uncertainty, so the Füchtbauer–Ladenburg (F-L) equation [37] was additionally employed. We used the following values of the radiative lifetime of the $^2\text{F}_{5/2}$ state giving a good agreement between the two methods: $\tau_{\text{rad}} = 1.01$ ms ($\text{Yb}:\text{Lu}_3\text{Al}_5\text{O}_{12}$) and 0.805 ms ($\text{Yb}:\text{Lu}_2\text{O}_3$) which agrees well with previous studies [24,38].

For $\text{Yb}:\text{Lu}_3\text{Al}_5\text{O}_{12}$, the maximum σ_{SE} is 2.46×10^{-20} cm² at a wavelength of 1030.2 nm which is longer than the ZPL transition. For $\text{Yb}:\text{Lu}_2\text{O}_3$, the maximum σ_{SE} is 1.65×10^{-20} cm² at 976.2 nm (the ZPL). At longer wavelengths, where the laser operation is expected, the SE cross-sections are lower, namely 0.86×10^{-20} cm² at 1033.0 nm.

The Yb^{3+} ion represents a quasi-three-level laser scheme with reabsorption. The gain cross-sections, $\sigma_{\text{gain}} = \beta\sigma_{\text{SE}} - (1 - \beta)\sigma_{\text{abs}}$, are thus calculated to conclude about the expected laser wavelengths. Here, $\beta = N_2(^2\text{F}_{5/2})/N_{\text{Yb}}$ is the inversion ratio (N_2 is the fraction of Yb^{3+} ions in the upper laser level). The gain spectra are shown in Fig. 7(b),(d). For $\text{Yb}:\text{Lu}_3\text{Al}_5\text{O}_{12}$, the spectra are only weakly dependent on the inversion level showing a maximum at ~1030 nm and a gain bandwidth (FWHM) of 6.7 nm for $\beta = 0.20$. For $\text{Yb}:\text{Lu}_2\text{O}_3$, at small inversion ratios, $\beta < 0.10$, the local peak at ~1080 nm dominates in the spectra and for higher inversion ratios, another peak at 1033 nm appears. The gain bandwidth is 14.7 nm for $\beta = 0.20$.

The crystal-field splitting for $\text{Yb}^{3+}:\text{Lu}_3\text{Al}_5\text{O}_{12}$ ceramics was determined using the LT (6 K) absorption and luminescence studies, as shown in Fig. 8(a),(b). The spectra were interpreted using the Raman spectra (see Fig. 10) to assign the phonon sidebands (marked by “ $h\nu$ ”). Each $^{2S+1}\text{L}_J$ multiplet splits into $J + 1/2$ components numbered as $i = 0..3$ ($^2\text{F}_{7/2}$, ground-state) and $j' = 0'..2'$ ($^2\text{F}_{5/2}$, excited-state). As a result, we determined the following set of energy levels: 0, 602, 643 and 764 cm⁻¹ ($^2\text{F}_{7/2}$), 10333, 10643 and 10908 cm⁻¹ ($^2\text{F}_{5/2}$), Fig. 8(c). Thus, $E_{\text{ZPL}} = 10333$ cm⁻¹ and the partition functions $Z_1 = 1.122$ and $Z_2 = 1.277$, so that $Z_1/Z_2 = 0.879$. The determined Stark splitting is close to that reported previously for highly-doped (15 at.%) $\text{Yb}:\text{Lu}_3\text{Al}_5\text{O}_{12}$ single-crystal, i.e., 0, 600, 635 and 762 cm⁻¹ ($^2\text{F}_{7/2}$), 10330, 10645 and 10900 cm⁻¹ ($^2\text{F}_{5/2}$) [24].

For both studied ceramics, the decay curves are clearly single-exponential, Fig. 9, corresponding to the luminescence lifetimes $\tau_{\text{lum}} = 1.01$ ms (for $\text{Yb}:\text{Lu}_3\text{Al}_5\text{O}_{12}$) and 0.74 ms (for $\text{Yb}:\text{Lu}_2\text{O}_3$).

The RT Raman spectra are shown in Fig. 10. The cubic garnet structure of $\text{Lu}_3\text{Al}_5\text{O}_{12}$ gives rise to 25 Raman-active modes (irreducible representations: $3\text{A}_{1g} + 8\text{E}_g + 14\text{F}_{2g}$) [39]. The most intense band at 374 cm⁻¹ assigned as A_{1g} (FWHM = 11 cm⁻¹) is due to the rotation of the $[\text{AlO}_4]$ tetrahedral unit. The second intense mode at 796 cm⁻¹ (also A_{1g} , FWHM = 14 cm⁻¹) is due to the breathing mode of the $[\text{AlO}_4]$ tetrahedrons. The maximum phonon energy is 869 cm⁻¹. The cubic sesquioxide structure of Lu_2O_3 has 22 Raman-active modes ($4\text{A}_g + 4\text{E}_g + 14\text{F}_g$) [40]. The most prominent band at 389 cm⁻¹ (FWHM = 11 cm⁻¹) is ascribed to the $\text{A}_g + \text{F}_g$ vibrations and the maximum phonon energy is ~610 cm⁻¹.

5. Laser operation

5.1 Laser set-up

For the laser experiments, we fabricated two rectangular ceramic elements with the following dimensions: Yb:Lu₃Al₅O₁₂ ($t = 2.75(z)$ mm, aperture: $3.18(x) \times 1.50$ mm²) and Yb:Lu₂O₃ ($t = 1.07(z)$ mm, aperture: $2.5(x) \times 2.5$ mm²), where x denotes an arbitrary direction lies in the plane of the ceramic disk and z -axis is orthogonal to it, respectively, cf. Fig. 1. Their input and output facets were polished to laser-grade quality and remained uncoated. The elements were wrapped in an Indium foil and mounted in a Cu-holder for better heat removal from all four lateral sides. The holder was cooled by circulating water (12 °C). The elements were placed in a compact (microchip-type) laser cavity formed by a flat pump mirror (PM) providing high transmission (HT) at ~ 0.97 μ m and high reflectance (HR) at 1.02–1.23 μ m, and a set of flat output couplers (OCs) with a transmission $T_{oc} = 0.5\%$ -10% at 1.02-1.10 μ m, Fig. 11. The PM and the OC were placed close to the laser element so that the geometrical cavity length was close to the element thickness. The mode stabilization in a plano-plano cavity was provided by the positive thermal lens in both materials.

The pump source was a fiber-coupled (N.A. = 0.22, fiber core diameter: 105 μ m) InGaAs laser diode (LD) emitting up to 54 W of unpolarized output at 968 nm (emission linewidth: 1.5 nm, $M^2 \approx 37$). Thus, the pumping was at the ZPL of Yb³⁺ ions in Lu₃Al₅O₁₂ ceramics. This approach (compared to pumping at 936 nm [25]) has the advantage of reduced heat load. The pump was reimaged into the ceramic by an antireflection (AR) coated 1:1 lens assembly ($f = 30$ mm) leading to a pump spot diameter $2w_p \approx 100$ μ m and a confocal parameter $2z_R \approx 1$ mm (in the gain element). The OCs provided high reflection at the pump wavelength ($R > 90\%$), so that the pumping was in a double-pass increasing the total pump absorption. The latter was determined from pump-transmission measurements at the laser threshold, $\eta_{abs}(2 \text{ passes}) = 25.5 \pm 1\%$ (for Yb:Lu₃Al₅O₁₂) and $19.9 \pm 1\%$ (Yb:Lu₂O₃). It was possible to operate the diode in quasi-CW regime by electronic modulation of the driving current.

The size of the laser mode in the ceramic laser element $2w_L$ was calculated using the ABCD formalism accounting for the thermal lens to be 55 ± 7 μ m (for Yb:Lu₃Al₅O₁₂) and 47 ± 5 μ m (for Yb:Lu₂O₃).

The laser output was separated from the residual pump using a long-pass filter (FEL1000, Thorlabs). The spectra were measured using a spectrometer (APE, WaveScan; 800-1600 nm).

5.2 Laser performance

First, we studied the performance of the Yb:Lu₃Al₅O₁₂ ceramics limiting the absorbed pump power to $P_{abs} < 5$ W, Fig. 12(a). Under such conditions, we did not observe any thermal effects (e.g., roll-over in the output dependence) when operating the laser in true CW regime. For the highest available output coupling ($T_{oc} = 10\%$), the laser generated 2.72 W at 1031.1 nm with a slope efficiency $\eta = 67.2\%$. The optical-to-optical efficiency η_{opt} vs. the pump power incident on the ceramic element was only 15.0%, mostly because of the limited pump

absorption. The laser threshold slightly increased with the output coupling, from $P_{th} = 0.30$ W (for $T_{OC} = 0.5\%$) to 0.45 W (for $T_{OC} = 10\%$).

The laser spectra were weakly dependent on the output coupling, Fig. 12(b). The laser oscillation occurred at ~ 1030 nm in agreement with the gain spectra, Fig. 7(b). The laser emission was unpolarized. The multi-line structure of the emission spectra is due to etalon (Fabry-Perot) effects at the interfaces of the laser element / cavity mirrors.

The Yb:Lu₃Al₅O₁₂ ceramic laser operated in the fundamental transverse mode. The example profile of the laser mode (measured using $T_{OC} = 10\%$) in the far-field is shown in Fig. 11(b). It is nearly circular. For $P_{abs} < 5$ W, the beam profile was weakly dependent on the pump level.

The performance of the Yb:Lu₃Al₅O₁₂ ceramic laser for $T_{OC} = 10\%$ was analyzed using the model of a quasi-three-level gain medium [41] yielding a double-pass intracavity loss L of 4.1%. This value is lower than the Fresnel losses at the uncoated surfaces of the laser element as it was polished with a good parallelism thus acting as a Fabry-Perot etalon. Thus, the coefficient of passive losses $\delta_{loss} = 0.076 \pm 0.05$ cm⁻¹.

For the Yb:Lu₂O₃ ceramics, we limited the absorbed pump power to $P_{abs} < 2$ W. The laser generated a maximum output power of 0.59 W at 1080-1084 nm with $\eta = 38.0\%$ and the optical-to-optical efficiency η_{opt} of 5.8% ($T_{OC} = 5\%$). The laser threshold gradually increased with the output coupling, from $P_{th} = 0.22$ W (for $T_{OC} = 0.5\%$) to 0.48 W (for $T_{OC} = 10\%$). A reduction in the laser threshold for small output coupling, as compared to the Yb:Lu₃Al₅O₁₂ laser is due to the smaller thickness of the Yb:Lu₂O₃ laser element. A thermal roll-over was observed in the output dependences for $P_{abs} > 2$ W. The emission occurred at ~ 1080 nm for low $T_{OC} \leq 5\%$ and the laser wavelength experienced a blue-shift to 1036 nm for higher T_{OC} , in agreement with the gain spectra, Fig. 7(d).

A notable reduction in the slope efficiency for the Yb:Lu₂O₃ laser as compared to its garnet counterpart is mainly attributed to non-optimum mode-matching owing to the shorter cavity and thermal lens. To confirm this, we designed a hemispherical laser cavity with a concave (radius of curvature: -50 mm) output coupler. The calculated size of the laser mode in the ceramic element for this cavity geometry amounted to 55 ± 5 μ m, i.e., much closer to the pump spot size. The CW output power reached 1.0 W at 1083 nm with $\eta = 68.0\%$ and a laser threshold of 0.28 W, see Fig. 12(c). Still, we were unable to avoid the thermal roll-over at $P_{abs} > 2$ W. The analysis of the laser performance yielded a double-pass loss L of 1.6% corresponding to $\delta_{loss} = 0.077 \pm 0.05$ cm⁻¹ (i.e., almost the same as for the garnet ceramics). Thus, the difference in the power scaling capabilities for the two ceramics is mainly related to their different thermal behavior. One should also consider much longer emission wavelength for the Yb:Lu₂O₃ ceramics leading to higher fractional heat loading, $\eta_h \approx 1 - \lambda_P/\lambda_L = 10.6\%$ (cf. with 6.1% for Yb:Lu₃Al₅O₁₂).

Subsequently the pump power for the Yb:Lu₃Al₅O₁₂ ceramic micro-laser was increased to the maximum available from the laser diode, Fig. 13(a). It corresponded to $P_{abs} = 13.7$ W. In the CW regime, the laser generated 5.65 W. As a result of the thermal roll-over in the input-output dependence for $P_{abs} > 5$ W, η_{opt} dropped to 10.5%. To reduce the heat loading, the laser was operated in quasi-CW regime with different duty cycles (from 1:1.5 to 1:3). The

duration of the rectangular pump pulses was 1 ms in all cases. With increasing the time interval between the pump pulses, the peak output power increased and the input-output dependence became linear reaching maximum values of $P_{\text{out,peak}} = 8.83$ W and $\eta = 66.9\%$, respectively, almost reproducing the slope of the true CW performance in the low-power regime.

To improve the thermal management of the ceramic laser, we also fabricated a slab-shaped Yb:Lu₃Al₅O₁₂ element with a thickness of 3.18(x) mm and aperture of 1.0(z)×2.75 mm². Cooling was provided at the two large-area lateral faces. The pump absorption in the slab slightly increased to 28.8±1% (2 passes). The input-output characteristics of the microslab ceramic laser are shown in Fig. 13(b) and compared with those for the microchip design. In the CW regime, the mini-slab laser generated 5.0 W at 1031.2 nm with improved $\eta = 78.8\%$ (fitting the linear part of the output dependence), a laser threshold of 0.58 W and $\eta_{\text{opt}} = 15.0\%$ ($T_{\text{oc}} = 10\%$). Still, a thermal roll-over was observed for P_{abs} above ~6 W. We assign the improved slope efficiency to better mode-matching and probably weaker thermal lens in the laser element owing to its better cooling.

Note that the cut of the ceramic laser element (i.e., the propagation direction of the laser) of the micro-laser was orthogonal to the plane of the ceramic disk (\parallel z-axis) while the cut of the slab element was lying on the plane of the disk (\parallel x-axis, see Fig. 1). No deterioration of the laser performance is observed in the latter case, indicating good uniformity of the ceramic disk in the radial direction and highlighting its suitability for laser applications. Transparent ceramics fabricated on the basis of cubic materials exhibit no anisotropy of optical properties. However, one may observe anisotropy of pore distribution in the ceramic disk (and, consequently, the related anisotropy of scattering losses) under synthesis conditions when the pores are predominantly removed along one direction, e.g., when using hot (uniaxial) pressing or spark plasma synthesis. The lack of such effects for the studied ceramics was confirmed by analyzing the distribution of scattering centers and the grain size distribution across the ceramic disks (the difference was within the measurement error).

5.3 Discussion

The present work reports the first CW laser operation of Yb:Lu₃Al₅O₁₂ and Yb:Lu₂O₃ ceramics obtained from laser-ablated nanoparticles.

Regarding previously reported Yb:Lu₃Al₅O₁₂ lasers based on single-crystals and ceramics, cf. Table 1, we obtained one of the best results in terms of output power (CW and quasi-CW operation) and slope efficiency, with highly compact (microchip-type) laser geometries. Microchip Yb:Lu₃Al₅O₁₂ lasers were reported by Dong *et al.* using 5 at.% Yb doped single-crystals delivering a maximum CW output power of 1.63 W at 1030 nm with $\eta = 72\%$. Much better output performance is achieved in the present work with the new ceramic material.

Using Yb:Lu₂O₃ ceramics, multi-watt CW laser output has been previously reported by other researchers, e.g., Sanghera *et al.* demonstrated a diode-pumped 10 at.% Yb:Lu₂O₃ laser

delivering ~16 W at 1080 nm with $\eta = 74\%$ [44]. However, a much larger pump spot size (as compared to the present work) was used thus reducing the localized heat release.

Let us discuss the reasons for the thermal roll-over observed for the Yb:Lu₂O₃ ceramic laser. The thermal conductivity of Yb:Lu₂O₃ ceramics is high ($\kappa = 13.9 \text{ Wm}^{-1}\text{K}^{-1}$ for 3 at.% Yb doping [10]) and is weakly dependent on the Yb doping level [45]; moreover, it is higher than that for Yb:Lu₃Al₅O₁₂ [10]. This difference would compensate for the higher fractional heat load in Yb:Lu₂O₃ originating from the longer emission wavelength. As determined in the present work, the passive losses in both materials at the laser wavelength are very close. Thus, another mechanism should be the reason.

It was suggested that the interaction of Yb³⁺ laser-active ions with uncontrolled rare-earth impurities such as Tb³⁺, Ho³⁺ or Dy³⁺ may affect the output performance of Yb ceramic lasers [25,45]. Such ions are always present in the Yb₂O₃ and Lu₂O₃ raw materials. In addition, Yb²⁺ ions may play a similar role and act as quenching centers for Yb³⁺. Typically, Yb²⁺ ions formed during the synthesis in oxygen-deficient conditions are completely removed after annealing in air unless a charge compensation is present by a tetravalent impurity center such as Tb⁴⁺. Terbium is polyvalent and Tb⁴⁺ species can be formed during the oxidizing annealing preventing complete removal of Yb²⁺. Indeed, an unwanted energy transfer from Yb³⁺ ions to such impurity centers will lead to additional heat generation.

To clarify this issue, we measured the luminescence spectra of Yb³⁺-doped ceramics under excitation in the blue, Fig. 14(a), using the Renishaw inVia confocal Raman microscope. For the Yb:Lu₂O₃ ceramics, we observed intense characteristic emissions of Tb³⁺ ions owing to the $^5\text{D}_4 \rightarrow ^5\text{F}_J$ ($J = 5 \dots 0$) transitions in addition to Yb³⁺ emission at ~1 μm which was at least one order or magnitude more intense. The spectral shape of the Yb³⁺ luminescence well matched the one observed under near-IR excitation. Although Tb³⁺ does not exhibit energy-levels being resonant in energy with the excited-state of Yb³⁺ (the energy of the metastable Tb³⁺ state $^5\text{D}_4$ is ~20500 cm^{-1} whereas the energy of the Yb³⁺ excited-state $^2\text{F}_{5/2}$ is ~10000 cm^{-1}), the bidirectional energy-transfer (ET) between these ions is known. It involves Yb³⁺-Yb³⁺ ion pairs exhibiting an excited-state with an energy $2E(^2\text{F}_{5/2}) \sim 20000 \text{ cm}^{-1}$ leading either to cooperative sensitization ($2\text{Yb}^{3+} \rightarrow \text{Tb}^{3+}$ ET) [46] or cooperative down-conversion ($\text{Tb}^{3+} \rightarrow 2\text{Yb}^{3+}$ ET) [47]. The latter process is observed in our case.

Furthermore, we analyzed the effect of the form of the sesquioxide material on the $\text{Tb}^{3+} \rightarrow 2\text{Yb}^{3+}$ ET by comparing the luminescence spectra of three materials: a commercial Lu₂O₃ powder, an Yb:Lu₂O₃ nanopowder produced by laser ablation, sedimentation and calcination, and an Yb:Lu₂O₃ ceramic, Fig. 14(b). Almost no Yb³⁺ emission is observed in the commercial (undoped) powder. In the visible, apart from the rare-earth ion impurity emissions, broad bands originating from defect states appear. For the nanopowder, both kinds of visible emissions are suppressed while the ~1 μm emission appears suggesting weak ET. Finally, for the ceramic, the Yb³⁺ emission is enhanced by an order of magnitude and the visible emissions are further diminished indicating much stronger ET.

For the Yb:Lu₃Al₅O₁₂ ceramics, Fig. 14(a), similar Tb³⁺ emissions are observed but the ~1 μm Yb³⁺ luminescence is much weaker due to cooperative down-conversion. The latter suggests weaker effect of terbium impurity on Yb³⁺ laser performance. The rare-earth ion

density in sesquioxides is higher than in garnets (for the same at.%) which explains the higher content of Tb in Yb:Lu₂O₃. It is known that cooperative energy-transfer processes are particularly strong in sesquioxides [47]. Thus, Tb³⁺ species directly act as quenching centers. Tb⁴⁺ species are formed during annealing serving as charge compensators for Yb²⁺ ions but also acting as strong quenching centers. As a consequence the presence of Tb³⁺ and Tb⁴⁺ may be responsible for the observed thermal roll-over and explains the coloration of the fabricated Yb:Lu₂O₃ ceramics.

6. Conclusions

We presented a detailed comparative study of the microstructure, optical, vibronic and spectroscopic properties, and diode-pumped laser performance of two Yb-doped Lu-based oxide transparent ceramics, namely Yb:Lu₃Al₅O₁₂ (garnet) and Yb:Lu₂O₃ (sesquioxide). These ceramics were synthesized using the same nanopowders (Yb:Lu₂O₃ and Al₂O₃) produced by laser ablation by two different methods: solid-state reaction synthesis at 1800 °C for 5 h with a presence of a sintering aid (1 wt% TEOS) and vacuum pre-sintering followed by HIP at 207 MPa / 1400 °C for 2 h, respectively. The use of different methods was dictated by the different microstructure evolution of these materials during sintering (concerning the pore formation) and it led to a notable difference in the mean grain size: 14 and 0.4 μm for Yb:Lu₃Al₅O₁₂ and Yb:Lu₂O₃, respectively. Both ceramics exhibited low content of μm-sized pores, a close-packed structure, high transmission at ~1.1 μm approaching the theoretical one, and relatively low passive losses at the Yb³⁺ laser wavelength.

Efficient continuous-wave laser operation under diode-pumping at 968 nm is achieved with both ceramics. The Yb:Lu₃Al₅O₁₂ ceramic outperformed its sesquioxide counterpart: a compact (microchip-type) laser generated 5.65 W at 1031.1 nm with a slope efficiency of 67.2% (fitting the linear part of the output dependence) and a laser threshold of 0.45 W and in the quasi-CW regime, the peak power was scaled up to 8.83 W (limited only by the available pump power). For the Yb:Lu₂O₃ ceramic laser, the power scaling was limited (the CW output power reached 1.0 W at 1083 nm with $\eta = 68.0\%$) by the thermo-optic effects which are assigned to stronger heat dissipation due in part to the longer laser wavelength and in part to the impurity Tb³⁺ ions and possibly Yb²⁺ ions charge-compensation by Tb⁴⁺ species. These optical centers also determined a weak brown coloration of the Yb:Lu₂O₃ ceramics.

Further power scaling of compact lasers based on both Lu-based oxide ceramics seems to be possible via several routes: (i) improvement of the ceramic quality by eliminating the effect of terbium impurity responsible for the formation of Tb³⁺ and Yb²⁺ centers, e.g., by purification of the nanopowders; (b) alleviating thermal effects using larger pump spot size or employing other geometries of the laser element providing more efficient cooling (e.g., slab-shaped, as already demonstrated in the present work for Yb:Lu₃Al₅O₁₂ ceramics); (iii) using higher Yb doping levels up to 10 at.% for better pump absorption efficiency.

The developed Yb:Lu₃Al₅O₁₂ ceramics are promising for thin-disk lasers and amplifiers at ~1 μm.

Acknowledgments

This work was supported by the Spanish Government (project No. MAT2016-75716-C2-1-R (AEI/FEDER,UE)); Generalitat de Catalunya (project No. 2017SGR755); Government of the Russian Federation (state task project No. 0389-2016-0002 (2018–2020)); RFBR (Grant No. 19-03-00855). The authors gratefully acknowledge Vyacheslav V. Platonov and Egor V. Tikhonov from IEP UrB RAS for providing Yb:Lu₂O₃ and Al₂O₃ nanopowders. L. B. thanks Mikhail Baranov from ITMO University for the help with the SEM studies.

Declaration of competing interests

The authors declare that they have no known competing financial interests or personal relationships that could have appeared to influence the work reported in this paper.

References

1. S. F. Wang, J. Zhang, D. W. Luo, F. Gu, D. Y. Tang, Z. L. Dong, G. E. B. Tan, W. X. Que, T. S. Zhang, S. Li, L. B. Kong, Transparent ceramics: Processing, materials and applications, *Prog. Sol. State Chem.* 41(1-2) (2013) 20-54.
2. A. Ikesue, Y. L. Aung, Ceramic laser materials, *Nature Photon.* 2(12) (2008) 721-727.
3. A. Ikesue, T. Kinoshita, K. Kamata, K. Yoshida, Fabrication and optical properties of high-performance polycrystalline Nd:YAG ceramics for solid-state lasers, *J. Am. Ceram. Soc.* 78(4) (1995) 1033-2040.
4. H. Yagi, T. Yanagitani, K. Takaichi, K. Ueda, A. A. Kaminskii, Characterizations and laser performances of highly transparent Nd³⁺:Y₃Al₅O₁₂ laser ceramics, *Opt. Mater.* 29(10) (2007) 1258-1262.
5. J. Dong, A. Shirakawa, K. Ueda, H. Yagi, T. Yanagitani, A. A. Kaminskii, Laser-diode pumped heavy-doped Yb:YAG ceramic lasers, *Opt. Lett.* 32(13) (2007) 1890-1892.
6. D. Luo, J. Zhang, C. Xu, H. Yang, H. Lin, H. Zhu, D. Tang, Yb:LuAG laser ceramics: a promising high power laser gain medium, *Opt. Mater. Express* 2(10) (2012) 1425-1431.
7. O. L. Antipov, A. A. Novikov, N. G. Zakharov, A. P. Zinoviev, Optical properties and efficient laser oscillation at 2066 nm of novel Tm:Lu₂O₃ ceramics, *Opt. Mater. Express* 2(2) (2012) 183-189.
8. W. X. Zhang, J. Zhou, W. B. Liu, J. Li, L. Wang, B. X. Jiang, Y. B. Pan, X. J. Cheng, J. Q. Xu, Fabrication, properties and laser performance of Ho:YAG transparent ceramic, *J. Alloy Compd.* 506(2) (2010) 745-748.
9. J. Lu, M. Prabhu, J. Song, C. Li, J. Xu, K. Ueda, A. A. Kaminskii, H. Yagi, T. Yanagitani, Optical properties and highly efficient laser oscillation of Nd:YAG ceramics, *Appl. Phys. B* 71(4) (2000) 469-473.
10. H. Nakao, T. Inagaki, A. Shirakawa, K. Ueda, H. Yagi, T. Yanagitani, A. A. Kaminskii, B. Weichelt, K. Wentsch, M. A. Ahmed, T. Graf, Yb³⁺-doped ceramic thin-disk lasers of Lu-based oxides, *Opt. Mater. Express* 4(10) (2014) 2116-2121.
11. J. Lu, J. Lu, T. Murai, K. Takaichi, T. Uematsu, K. Ueda, H. Yagi, T. Yanagitani, A. A. Kaminskii, Nd³⁺:Y₂O₃ ceramic laser, *Jpn. J. Appl. Phys.* 40(12A) (2001) L1277-L1279.

12. J. Lu, J. F. Bisson, K. Takaichi, T. Uematsu, A. Shirakawa, M. Musha, K. Ueda, H. Yagi, T. Yanagitani, A. A. Kaminskii, Yb³⁺:Sc₂O₃ ceramic laser, *Appl. Phys. Lett.* 83(6) (2003) 1101-1103.
13. W. Jing, P. Loiko, J. M. Serres, Y. Wang, E. Vilejshikova, M. Aguiló, F. Díaz, U. Griebner, H. Huang, V. Petrov, X. Mateos, Synthesis, spectroscopy, and efficient laser operation of “mixed” sesquioxide Tm:(Lu,Sc)₂O₃ transparent ceramics, *Opt. Mater. Express* 7(11) (2017) 4192-4202.
14. I. Shoji, S. Kurimura, Y. Sato, T. Taira, A. Ikesue, K. Yoshida, Optical properties and laser characteristics of highly Nd³⁺-doped Y₃Al₅O₁₂ ceramics, *Appl. Phys. Lett.* 77(7) (2000) 939-941.
15. G. Toci, A. Pirri, B. Patrizi, R. N. Maksimov, V. V. Osipov, V. A. Shitov, A. S. Yurovskikh, M. Vannini, High efficiency emission of a laser based on Yb-doped (Lu,Y)₂O₃ ceramic, *Opt. Mater.* 83 (2018) 182-186.
16. J. Kong, D. Y. Tang, B. Zhao, J. Lu, K. Ueda, H. Yagi, T. Yanagitani, 9.2-W diode-end-pumped Yb:Y₂O₃ ceramic laser, *Appl. Phys. Lett.* 86(16) (2005) 161116-1-3.
17. C. W. Xu, D. W. Luo, J. Zhang, H. Yang, X. P. Qin, W. D. Tan, D. Y. Tang, Diode pumped highly efficient Yb:Lu₃Al₅O₁₂ ceramic laser, *Laser Phys. Lett.* 9(1) (2012) 30-34.
18. H. Nakao, A. Shirakawa, K. Ueda, H. Yagi, and T. Yanagitani, CW and mode-locked operation of Yb³⁺-doped Lu₃Al₅O₁₂ ceramic laser, *Opt. Express* 20(14) (2012) 15385-15391.
19. M. Tokurakawa, A. Shirakawa, K. Ueda, H. Yagi, T. Yanagitani, A. A. Kaminskii, Diode-pumped sub-100 fs Kerr-lens mode-locked Yb³⁺:Sc₂O₃ ceramic laser, *Opt. Lett.* 32(23) (2007) 3382-3384.
20. M. Tokurakawa, A. Shirakawa, K. Ueda, H. Yagi, T. Yanagitani, A. A. Kaminskii, K. Beil, C. Kränkel, G. Huber, Continuous wave and mode-locked Yb³⁺:Y₂O₃ ceramic thin disk laser, *Opt. Express* 20(10) (2012) 10847-10853.
21. K. Beil, S. T. Fredrich-Thornton, F. Tellkamp, R. Peters, C. Kränkel, K. Petermann, G. Huber, Thermal and laser properties of Yb:LuAG for kW thin disk lasers, *Opt. Express* 18(20) (2010) 20712-20722.
22. Y. Fu, J. Li, C. Wang, T. Xie, W. Li, L. Wu, Y. Pan, Fabrication and properties of highly transparent Yb:LuAG ceramics, *J. Alloys Compd.* 664 (2016) 595-601.
23. D. Luo, J. Zhang, C. Xu, H. Yang, H. Lin, H. Zhu, D. Tang, Yb:LuAG laser ceramics: a promising high power laser gain medium, *Opt. Mater. Express* 2(10) (2012) 1425-1431.
24. A. Brenier, Y. Guyot, H. Canibano, G. Boulon, A. Ródenas, D. Jaque, A. Eganyan, A. G. Petrosyan, Growth, spectroscopic, and laser properties of Yb³⁺-doped Lu₃Al₅O₁₂ garnet crystal, *J. Opt. Soc. Am. B* 23(4) (2006) 676-683.
25. A. Pirri, M. Vannini, V. Babin, M. Nikl, G. Toci, CW and quasi-CW laser performance of 10 at.% Yb³⁺:LuAG ceramic, *Laser Phys.* 23(9) (2013) 095002-1-7.
26. L. Basyrova, R. Maksimov, V. Shitov, M. Baranov, V. Mikhaylovsky, A. Khubetsov, O. Dymshits, X. Mateos, P. Loiko, Effect of SiO₂ addition on structural and optical properties of Yb:Lu₃Al₅O₁₂ transparent ceramics based on laser ablated nanopowders, *J. Alloys Compd.* 806, (2019) 717-725.
27. V. S. Kijko, R. N. Maksimov, V. A. Shitov, S. L. Demakov, A. S. Yurovskikh, Sintering of transparent Yb-doped Lu₂O₃ ceramics using nanopowder produced by laser ablation method, *J. Alloys Compd.* 643 (2015) 207-211.

28. C. Ma, F. Tang, J. Zhu, M. Du, X. Yuan, Y. Yu, K. Wang, Z. Wen, J. Zhang, J. Long, W. Guo, Y. Cao, Spectral and laser properties of Yb:LuAG transparent ceramics fabricated by tape casting method, *J. Am. Ceram. Soc.* 99(10) (2016) 3267-3272.
29. W. H. Rhodes, Y. Wang, C. Brecher, and J. G. Baldoni, Loss and recovery of transparency in pressure-consolidated Lu₃Al₅O₁₂, *J. Am. Ceram. Soc.* 94(11) (2011) 3655-3658.
30. R. D. Shannon, Revised effective ionic radii and systematic studies of interatomic distances in halides and chalcogenides, *Acta Cryst. A* 32(5) (1976) 751-767.
31. M. Guzik, J. Pejchal, A. Yoshikawa, A. Ito, T. Goto, M. Siczek, T. Lis, G. Boulon, Structural investigations of Lu₂O₃ as single crystal and polycrystalline transparent ceramic, *Cryst. Growth Des.* 14(7) (2014) 3327-3334.
32. C. Kränkel, Rare-earth-doped sesquioxides for diode-pumped high-power lasers in the 1-, 2-, and 3- μ m spectral range, *IEEE J. Sel. Top. Quantum Electron.* 21(1) (2014) 250-262 (2014).
33. Y. Kuwano, K. Suda, N. Ishizawa, T. Yamada, Crystal growth and properties of (Lu,Y)₃Al₅O₁₂, *J. Cryst. Growth* 260(1-2) (2004) 159-164.
34. D. E. Zelmon, J. M. Northridge, N. D. Haynes, D. Perlov, K. Petermann, Temperature-dependent Sellmeier equations for rare-earth sesquioxides, *Appl. Opt.* 52(16) (2013) 3824-3828 (2013).
35. S. A. Payne, L. L. Chase, L. K. Smith, W. L. Kway, W. F. Krupke, Infrared cross-section measurements for crystals doped with Er³⁺, Tm³⁺ and Ho³⁺, *IEEE J. Quantum Electron.* 28(11) (1992) 2619-2630.
36. Y. Guyot, M. Guzik, G. Alombert-Goget, J. Pejchal, A. Yoshikawa, A. Ito, T. Goto, G. Boulon, Assignment of Yb³⁺ energy levels in the C₂ and C_{3i} centers of Lu₂O₃ sesquioxide either as ceramics or as crystal, *J. Lumin.* 170 (2016) 513-519.
37. B. Aull, H. Jansen, Vibronic interactions in Nd:YAG resulting in nonreciprocity of absorption and stimulated emission cross sections, *IEEE J. Quantum Electron.* 18(5) (1982) 925-930.
38. R. Peters, C. Kränkel, K. Petermann, G. Huber, Crystal growth by the heat exchanger method, spectroscopic characterization and laser operation of high-purity Yb:Lu₂O₃, *J. Cryst. Growth* 310(7-9) (2008) 1934-1938.
39. A. A. Kaminskii, H. Rhee, O. Lux, H. J. Eichler, S. N. Bagayev, H. Yagi, K. Ueda, A. Shirakawa, J. Dong, Stimulated Raman scattering in “garnet” Lu₃Al₅O₁₂ ceramics—a novel host-material for Ln- and TM-lasant ions, *Laser Phys. Lett.* 8(6) (2011) 458-464.
40. N. D. Todorov, M. V. Abrashev, V. Marinova, M. Kadiyski, L. Dimowa, E. Faulques, Raman spectroscopy and lattice dynamical calculations of Sc₂O₃ single crystals, *Phys. Rev. B* 87(10) (2013) 104301-1-5.
41. J. M. Serres, V. Jambunathan, P. Loiko, X. Mateos, H. Yu, H. Zhang, J. Liu, A. Lucianetti, T. Mocek, K. Yumashev, U. Griebner, V. Petrov, M. Aguiló, F. Díaz, Microchip laser operation of Yb-doped gallium garnets, *Opt. Mater. Express* 6(1) (2016) 46-57.
42. J. Dong, K. Ueda, A. A. Kaminskii, Laser-diode pumped efficient Yb:LuAG microchip lasers oscillating at 1030 and 1047 nm, *Laser Phys. Lett.* 7(10) (2010) 726-733.
43. A. Pirri, G. Toci, M. Nikl, V. Babin, M. Vannini, Experimental evidence of a nonlinear loss mechanism in highly doped Yb:LuAG crystal, *Opt. Express* 22(4) (2014) 4038-4049.

44. J. Sanghera, J. Frantz, W. Kim, G. Villalobos, C. Baker, B. Shaw, B. Sadowski, M. Hunt, F. Miklos, A. Lutz, I. Aggarwal, 10% Yb³⁺-Lu₂O₃ ceramic laser with 74% efficiency, *Opt. Lett.* 36(4) (2011) 576-578.
45. V. Peters, Growth and spectroscopy of ytterbium doped sesquioxides, PhD Thesis, Hamburg University, 2001.
46. A. Pandey, V. K. Rai, K. Kumar, Influence of Li⁺ codoping on visible emission of Y₂O₃:Tb³⁺, Yb³⁺ phosphor, *Spectrochim. Acta A* 118 (2014) 619-623.
47. J.-L. Yuan, X.-Y. Zeng, J.-T. Zhao, Z.-J. Zhang, H.-H. Chen, X.-X. Yang, Energy transfer mechanisms in Tb³⁺, Yb³⁺ codoped Y₂O₃ downconversion phosphor, *J. Phys. D: Appl. Phys.* 41(10) (2008) 105406-1-6.

List of figure captions

Figure 1. Photograph of Yb:Lu₃Al₅O₁₂ (*left*) and Yb:Lu₂O₃ (*right*) ceramic disks after annealing.

Figure 2. Effect of the annealing temperature and duration on the transmission of an Yb:Lu₂O₃ ceramic disk (thickness: $t = 1.0$ mm).

Figure 3. X-ray powder diffraction (XRD) patterns of (a) Yb:Lu₃Al₅O₁₂ and (b) Yb:Lu₂O₃ ceramics, *numbers* denote the Miller's indices (hkl). *Blue bars* – positions of the diffraction peaks for cubic Lu₃Al₅O₁₂ and Lu₂O₃ phases.

Figure 4. In-depth distribution of scattering centers in (a) Yb:Lu₃Al₅O₁₂ ($t = 1.75$ mm) and (b) Yb:Lu₂O₃ ($t = 1.4$ mm) ceramics.

Figure 5. Scanning Electron Microscopy (SEM) images of the fracture surface of (a) Yb:Lu₃Al₅O₁₂ and (b) Yb:Lu₂O₃ ceramics, *insets*: grain size distributions.

Figure 6. Low-signal transmission spectra of Yb:Lu₃Al₅O₁₂ and Yb:Lu₂O₃ ceramic disks ($t = 1.0$ mm), *dashed curves* - calculated Fresnel losses.

Figure 7. Room temperature spectroscopy of Yb³⁺ in (a,b) Lu₃Al₅O₁₂ and (c,d) Lu₂O₃ ceramics: (a,c) absorption, σ_{abs} , and stimulated-emission (SE), σ_{SE} , cross-section spectra for the ${}^2\text{F}_{5/2} \leftrightarrow {}^2\text{F}_{7/2}$ transition; (b,d) gain cross-sections, $\sigma_{\text{gain}} = \beta\sigma_{\text{SE}} - (1 - \beta)\sigma_{\text{abs}}$, where $\beta = N_2({}^2\text{F}_{5/2})/N_{\text{Yb}}$ is the inversion ratio and N_2 is the population of the upper laser level.

Figure 8. Low-temperature (6 K) spectroscopy of Yb³⁺ in Lu₃Al₅O₁₂ ceramics: (a) absorption spectrum, (b) luminescence spectrum, $\lambda_{\text{exc}} = 976$ nm. “ $h\nu$ ” – phonon sidebands; (c) Stark splitting of Yb³⁺ multiplets: $i = 0..3$ and $j' = 0'..2'$ number the Stark sub-levels, *values* indicate their energy in cm^{-1} , $Z_{1(2)}$ are the partition functions for the lower (upper) multiplets.

Figure 9. Room temperature luminescence decay curves of Yb³⁺ in (a) Lu₃Al₅O₁₂ and (b) Lu₂O₃ ceramics measured for powdered samples (plotted in a semi-log scale), *symbols*: experimental data, *lines*: their exponential fits, $\lambda_{\text{exc}} = 970$ nm, $\lambda_{\text{lum}} = 1050$ nm.

Figure 10. Room temperature Raman spectra of (a) Yb:Lu₃Al₅O₁₂ and (b) Yb:Lu₂O₃ ceramics, *numbers* denote the Raman frequencies in cm^{-1} . $\lambda_{\text{exc}} = 488$ nm.

Figure 11. (a) Scheme of the compact diode-pumped ytterbium ceramic laser: LD – laser diode, PM – pump mirror, OC – output coupler; (b) Typical profile of the output laser mode for the Yb:Lu₃Al₅O₁₂ ceramic laser.

Figure 12. Low-power diode-pumped laser performance of (a,b) 3.6 at.% Yb:Lu₃Al₅O₁₂ and (c,d) 3.6 at.% Yb:Lu₂O₃ ceramics (microchip laser geometry): (a,c) input-output dependences, η – slope efficiency; (b,d) typical laser emission spectra measured at $P_{\text{abs}} = 4$ W. In (c), the results for a hemispherical cavity are shown for comparison. The laser emission is unpolarized.

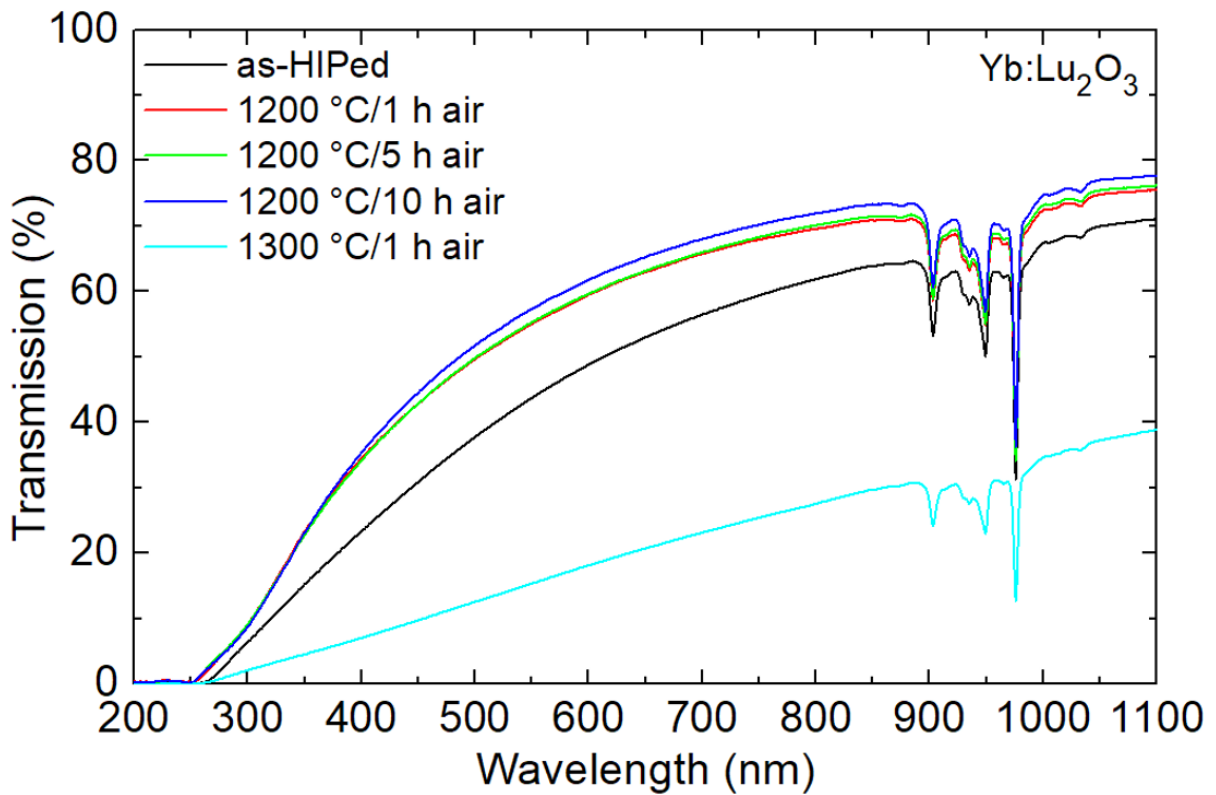
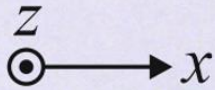
Figure 13. Thermal effects in the diode-pumped 3.6 at.% Yb:Lu₃Al₅O₁₂ ceramic lasers: (a) CW and quasi-CW performance of the microchip laser; (b) Comparison of the CW performance of the microchip laser and the mini-slab laser, η – slope efficiency, $T_{\text{OC}} = 10\%$.

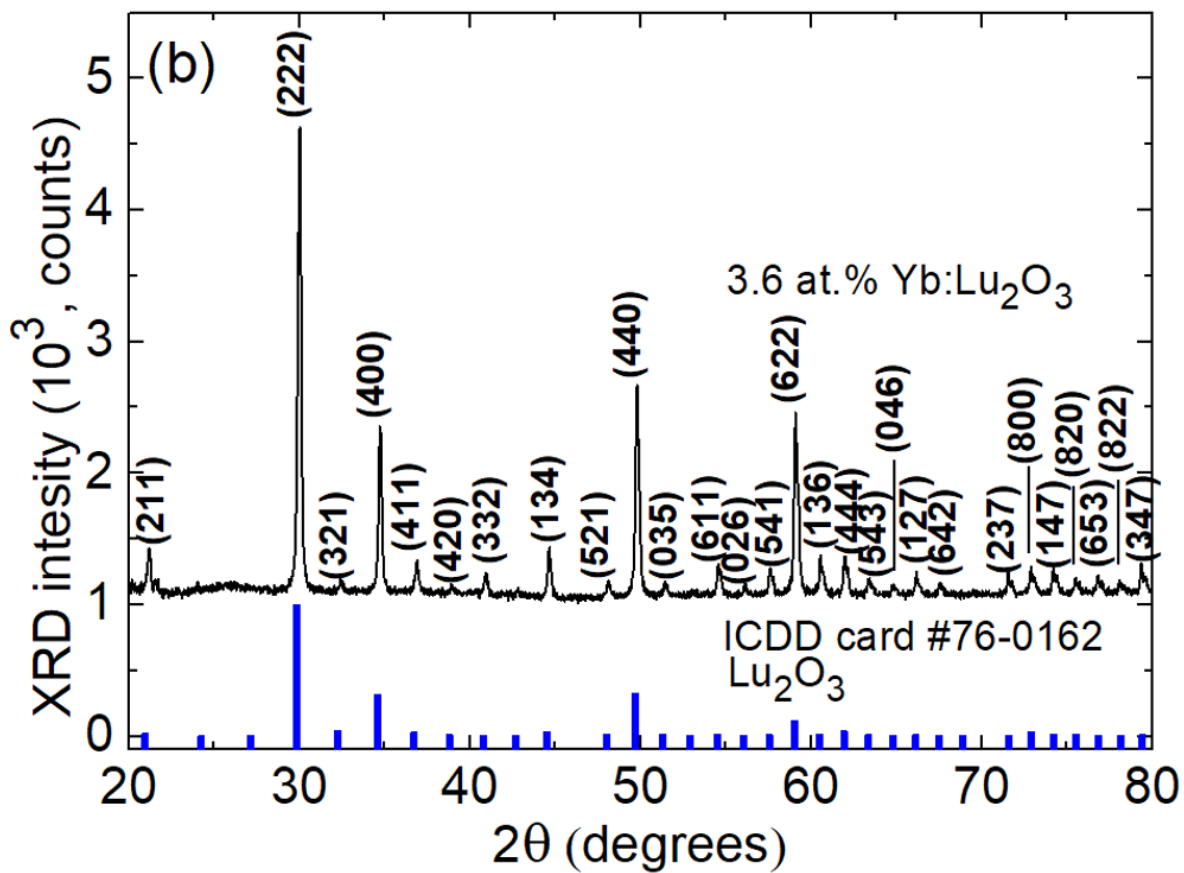
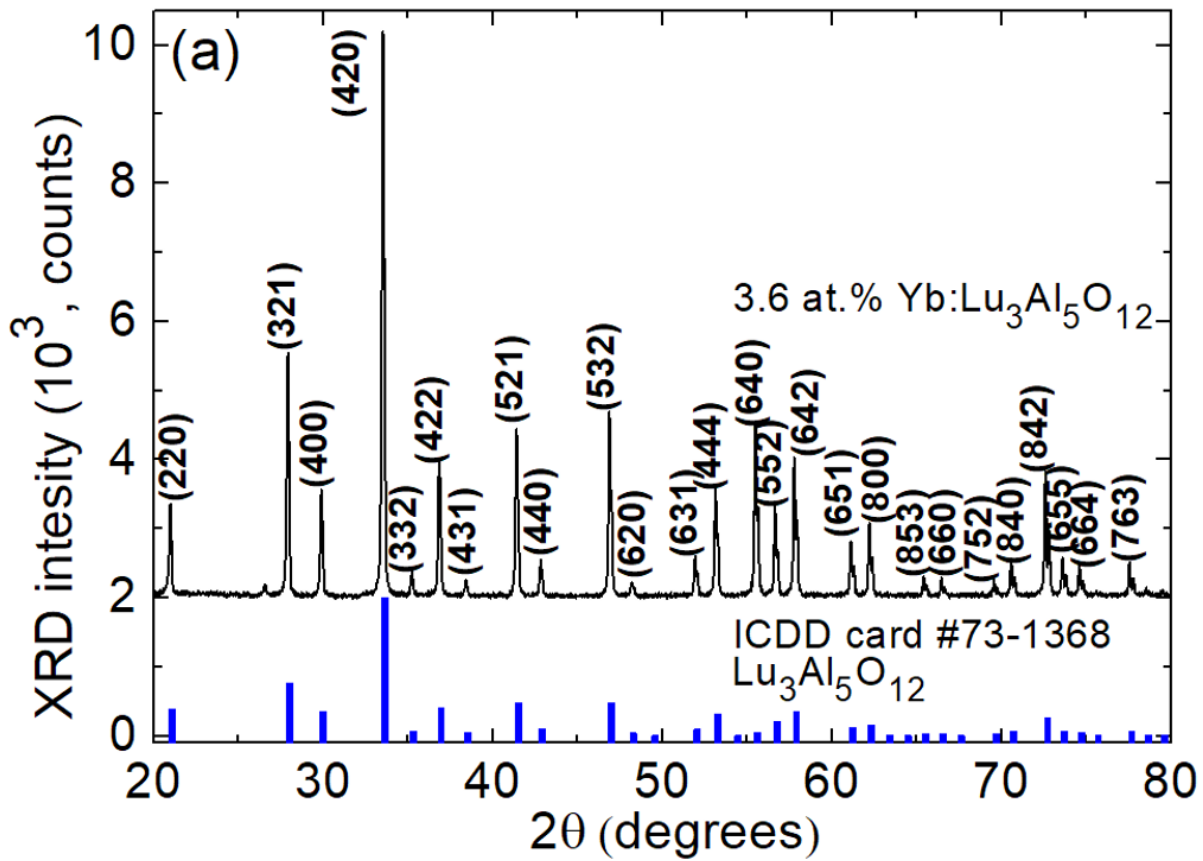
Figure 14. (a) Luminescence spectra of Yb:Lu₃Al₅O₁₂ and Yb:Lu₂O₃ ceramics under excitation in the blue. The spectra are normalized with respect to the visible emission. For the Yb:Lu₂O₃ ceramic, the ~ 1 μm luminescence is divided by a factor of 10; (b) Luminescence spectra of a commercial Lu₂O₃ powder, laser-ablated and calcined Yb:Lu₂O₃ nanopowder, and Yb:Lu₂O₃ ceramic.

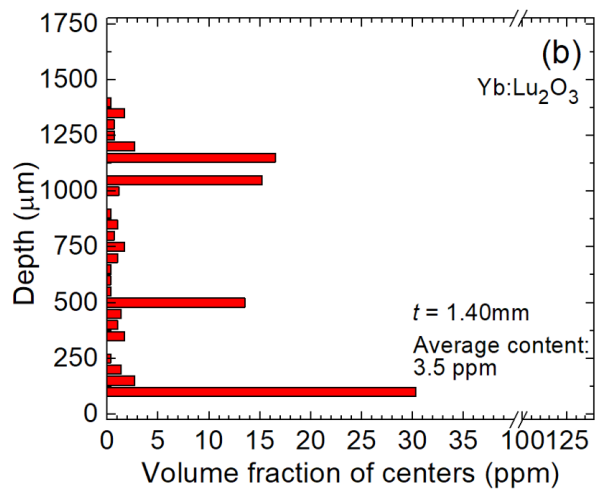
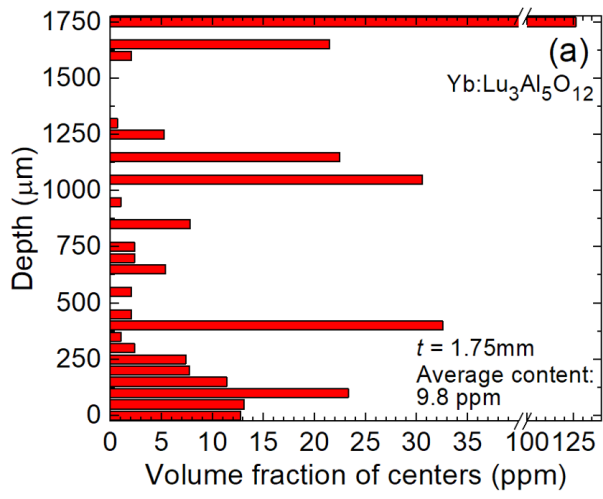


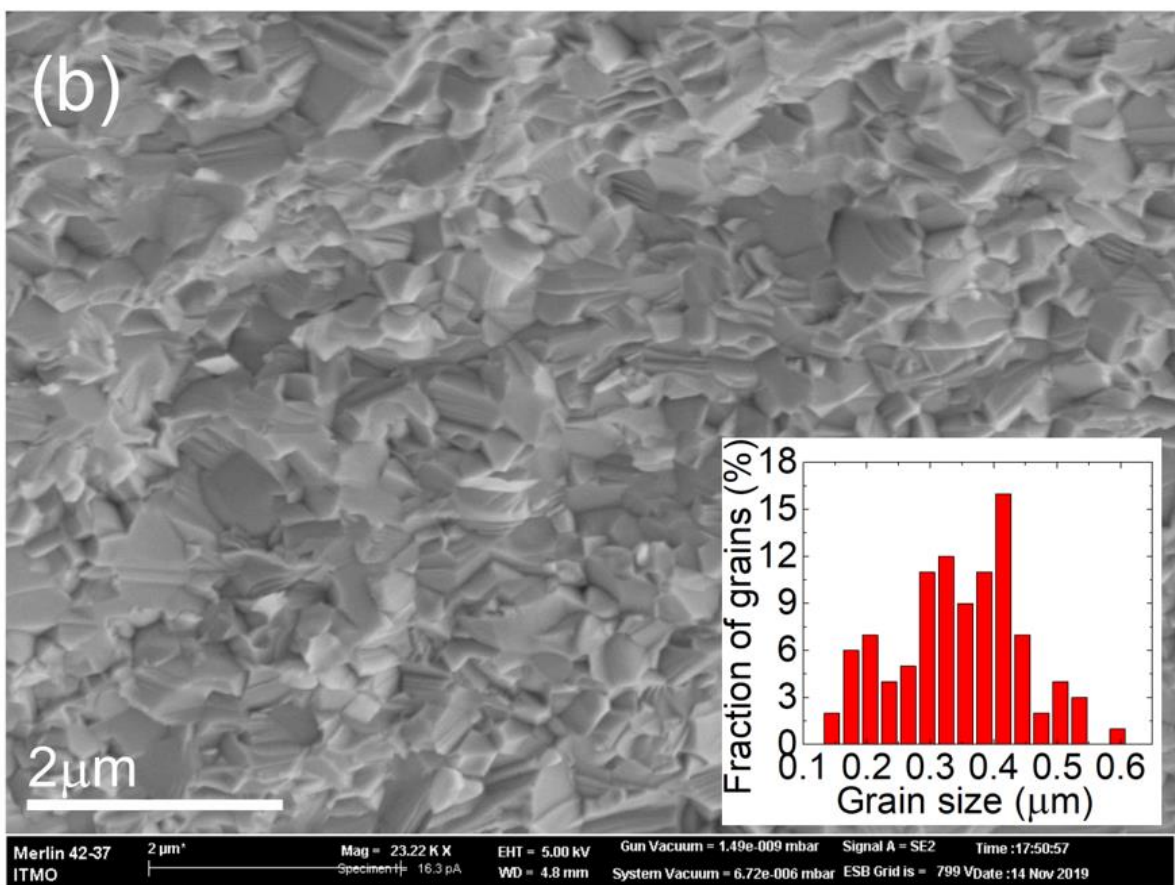
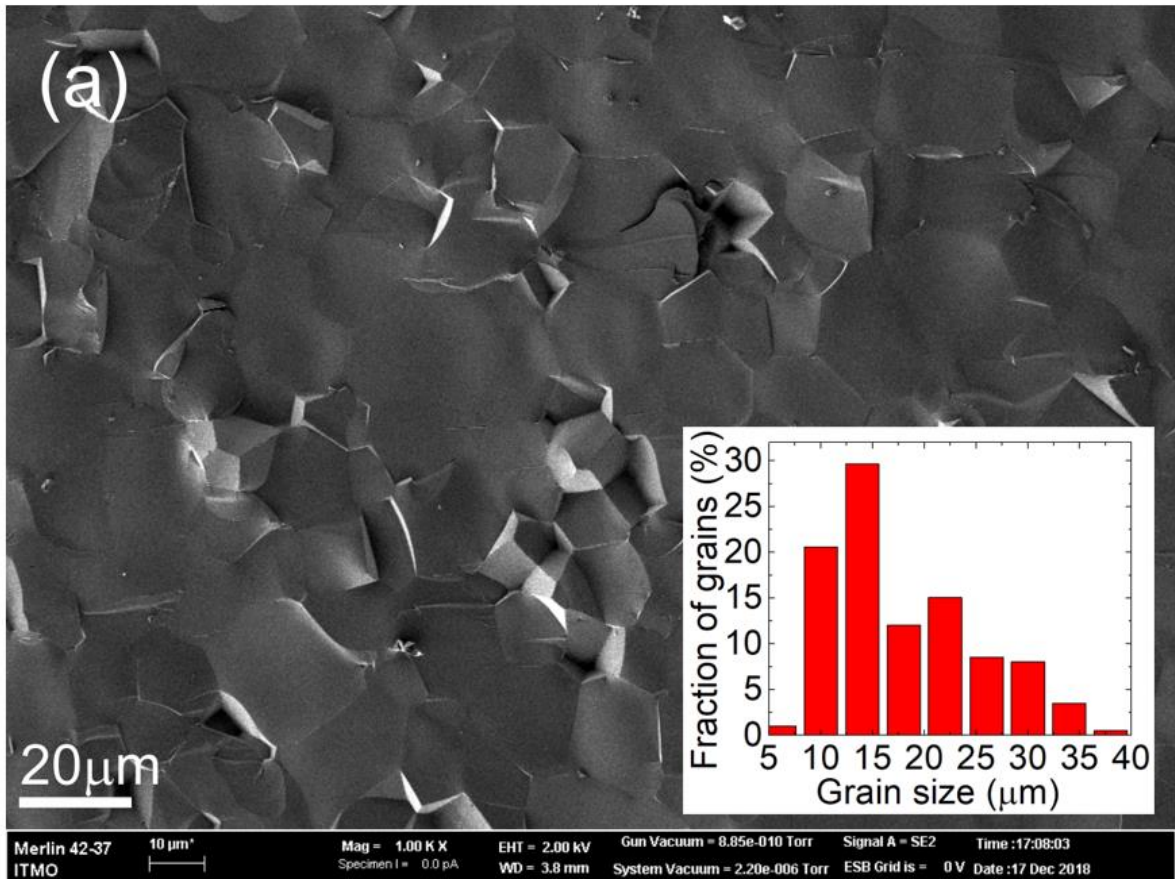
Yb:Lu₃Al₅O₁₂

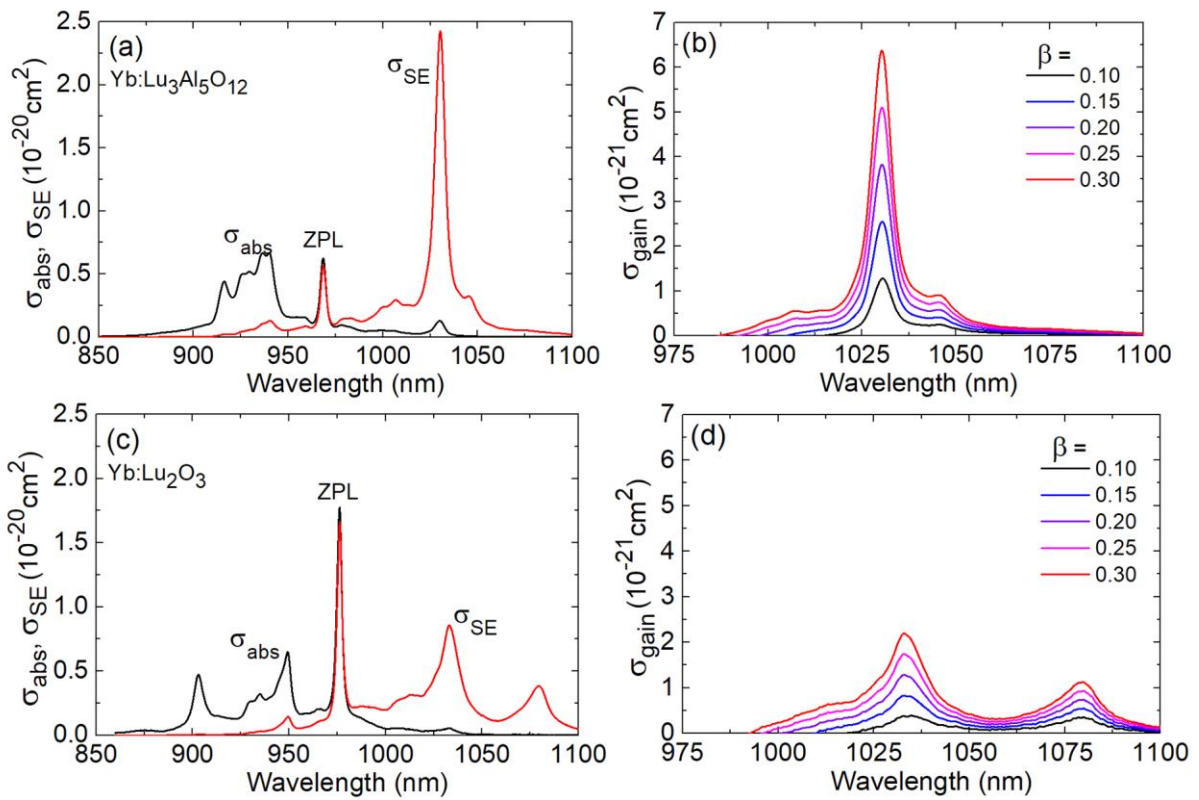
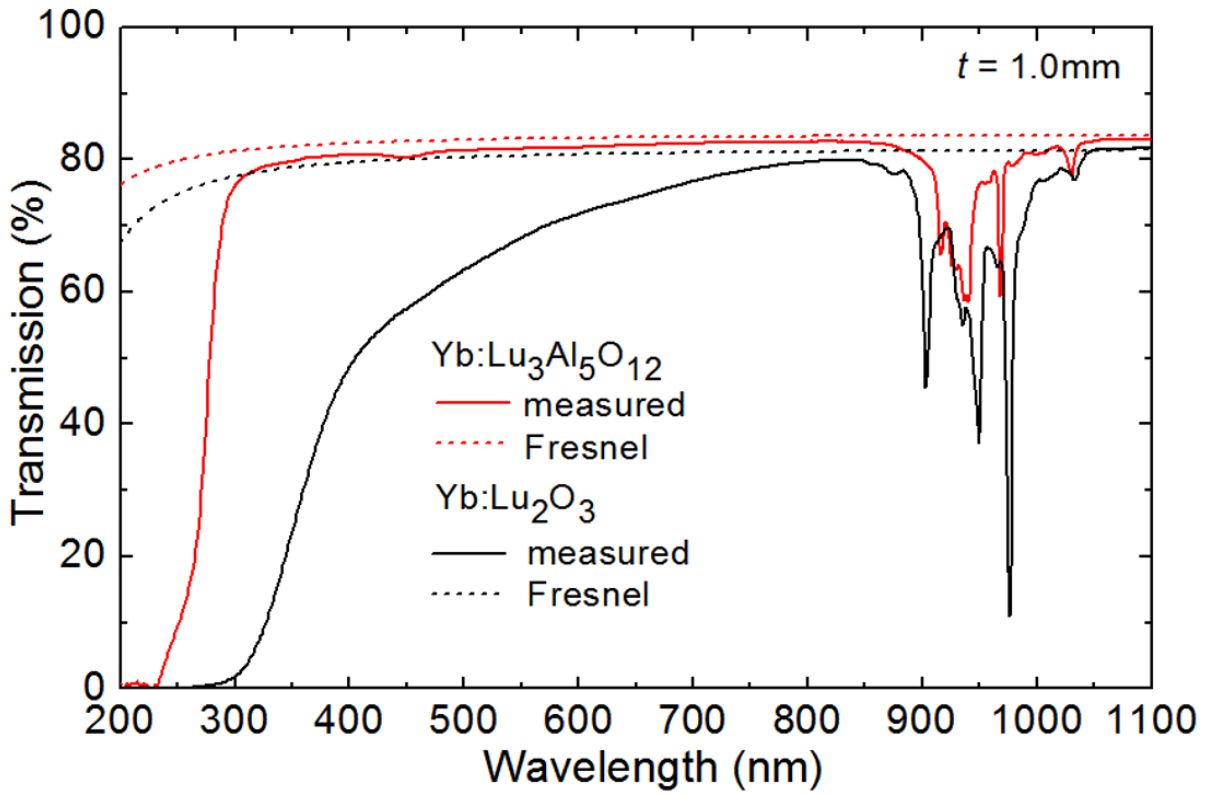
Yb:Lu₂O₃

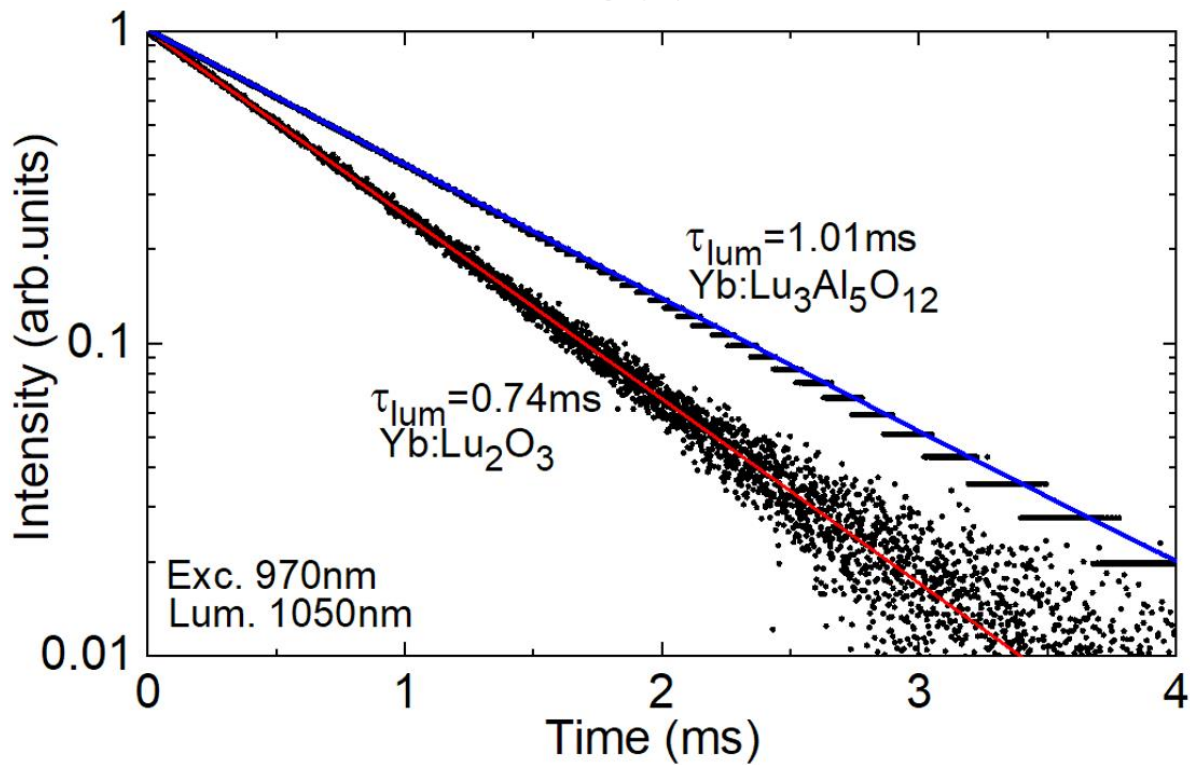
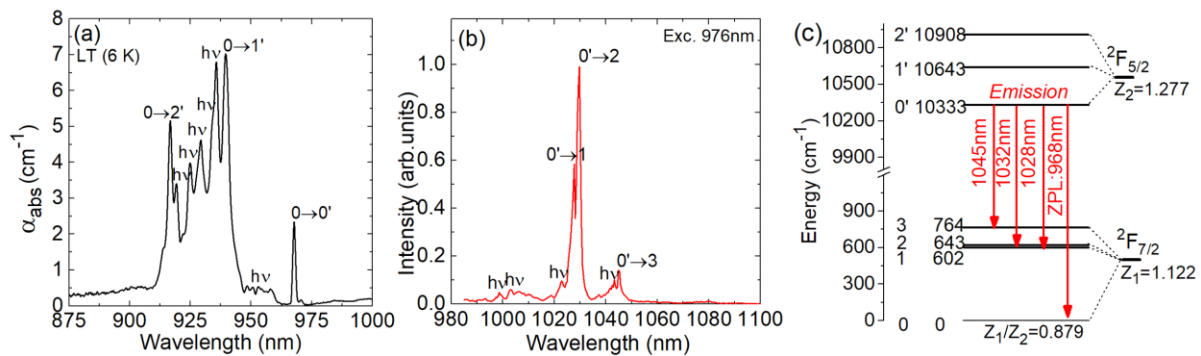


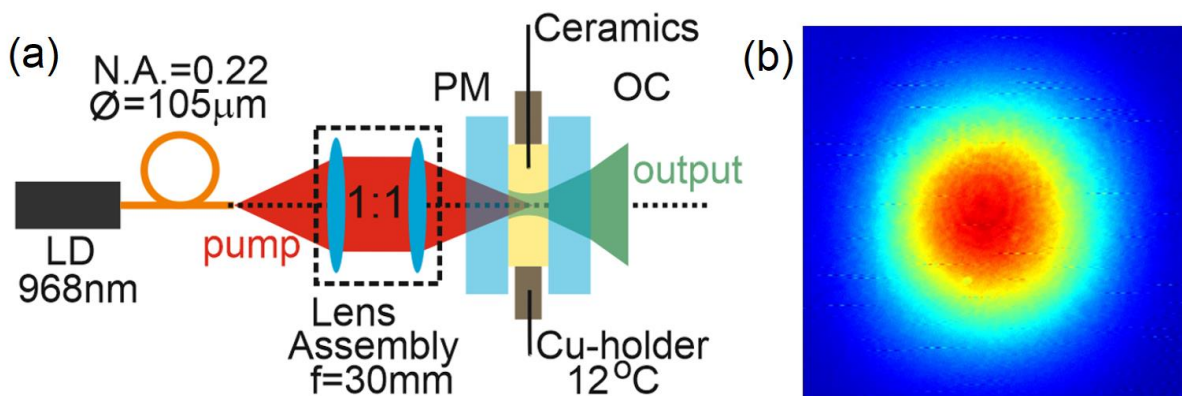
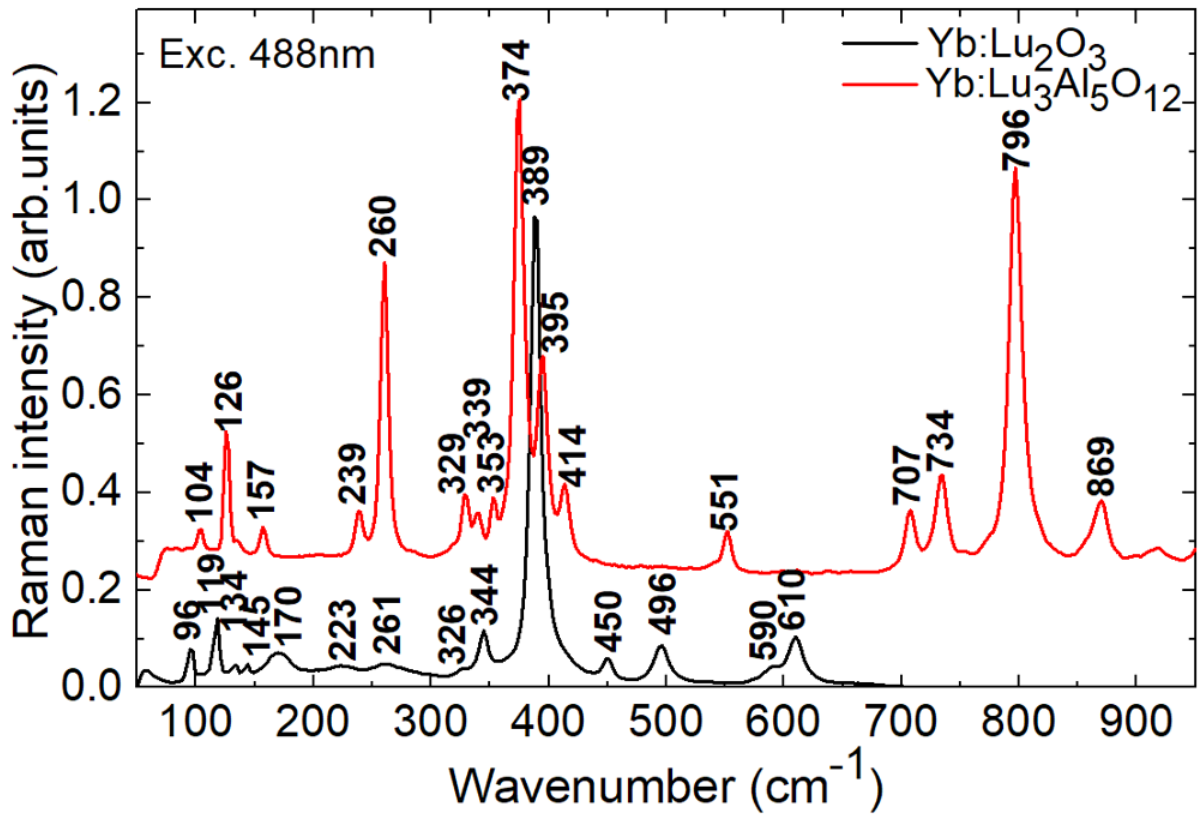


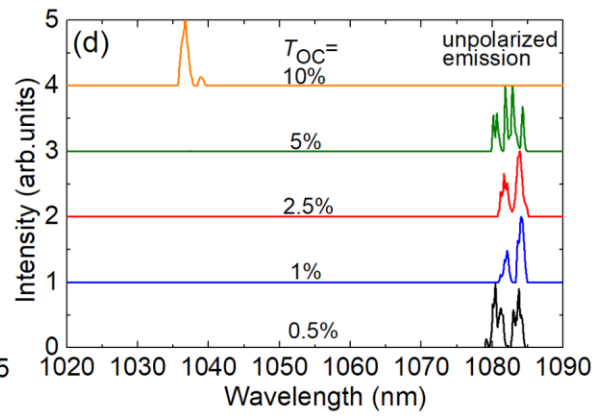
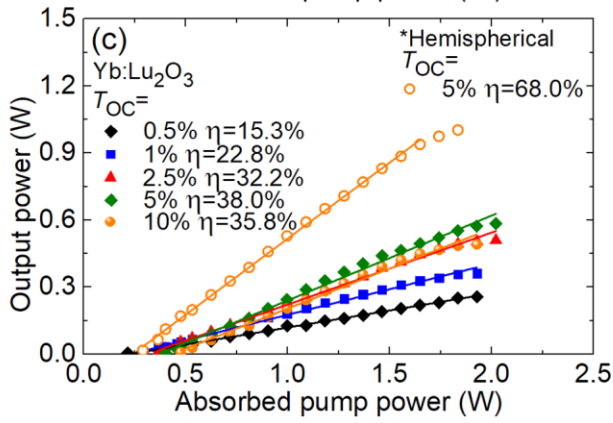
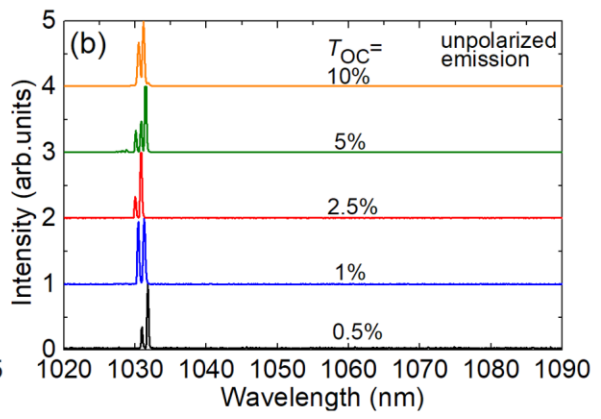
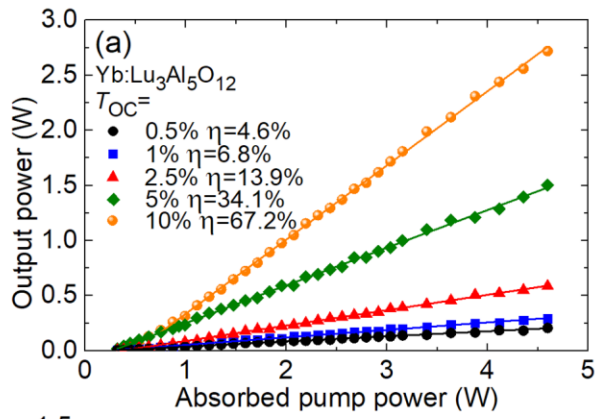


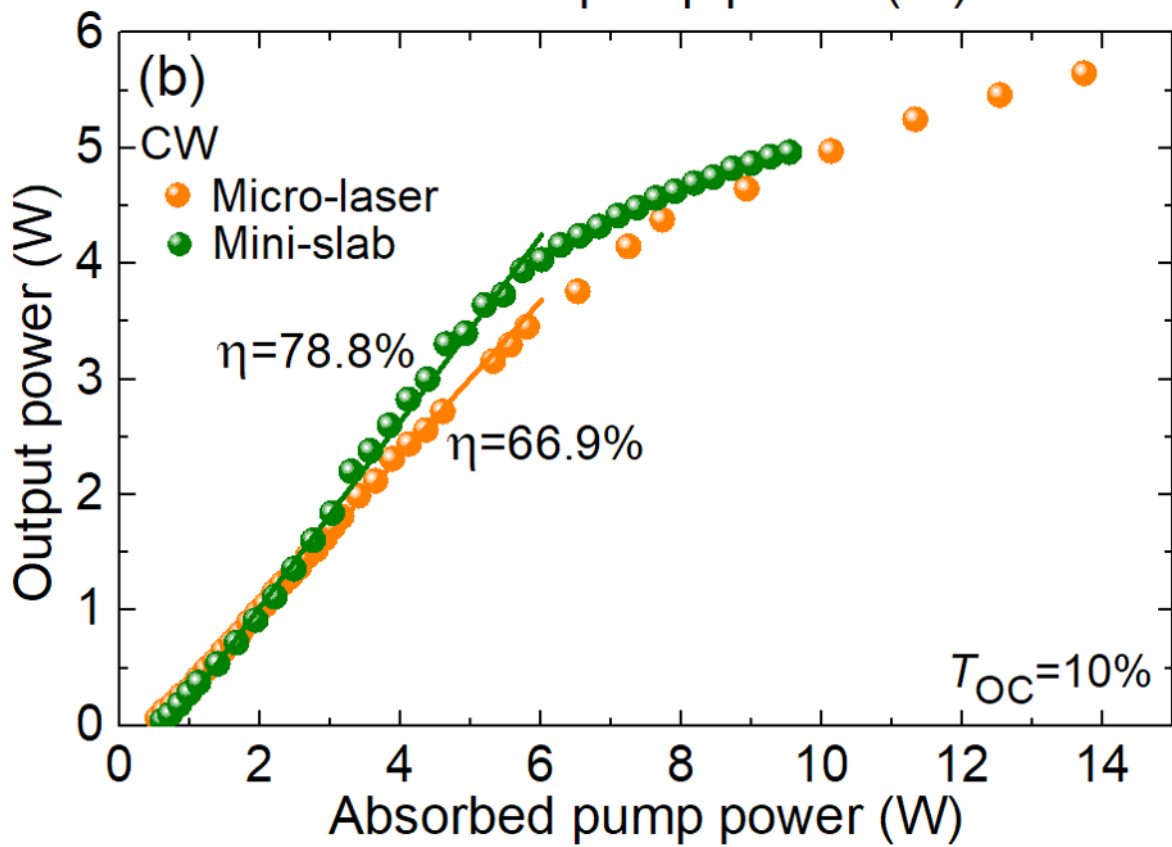
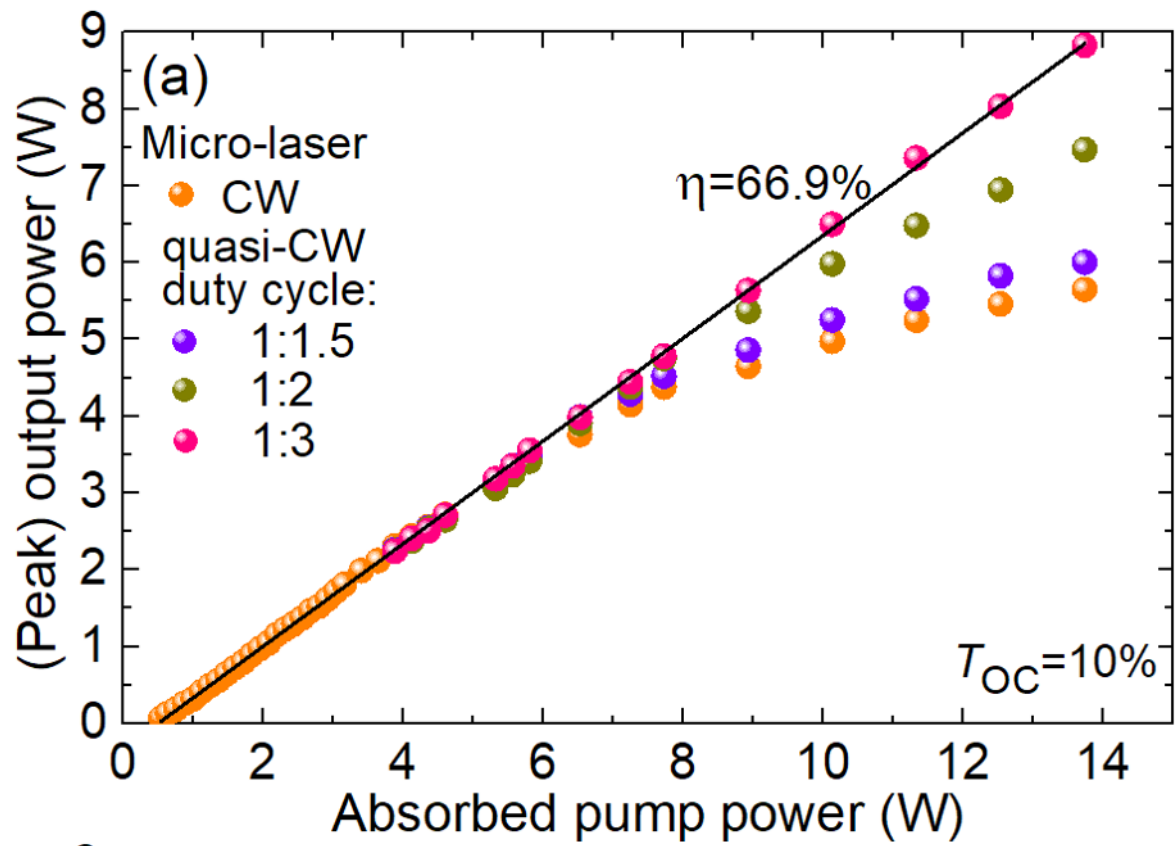












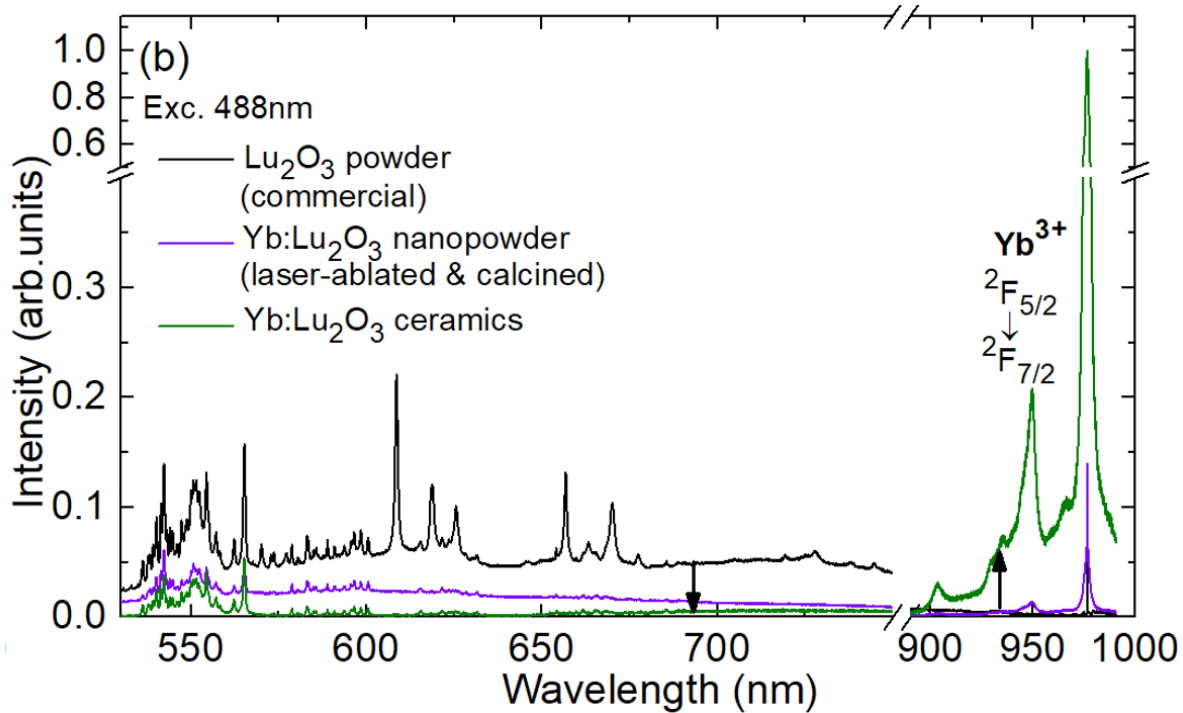
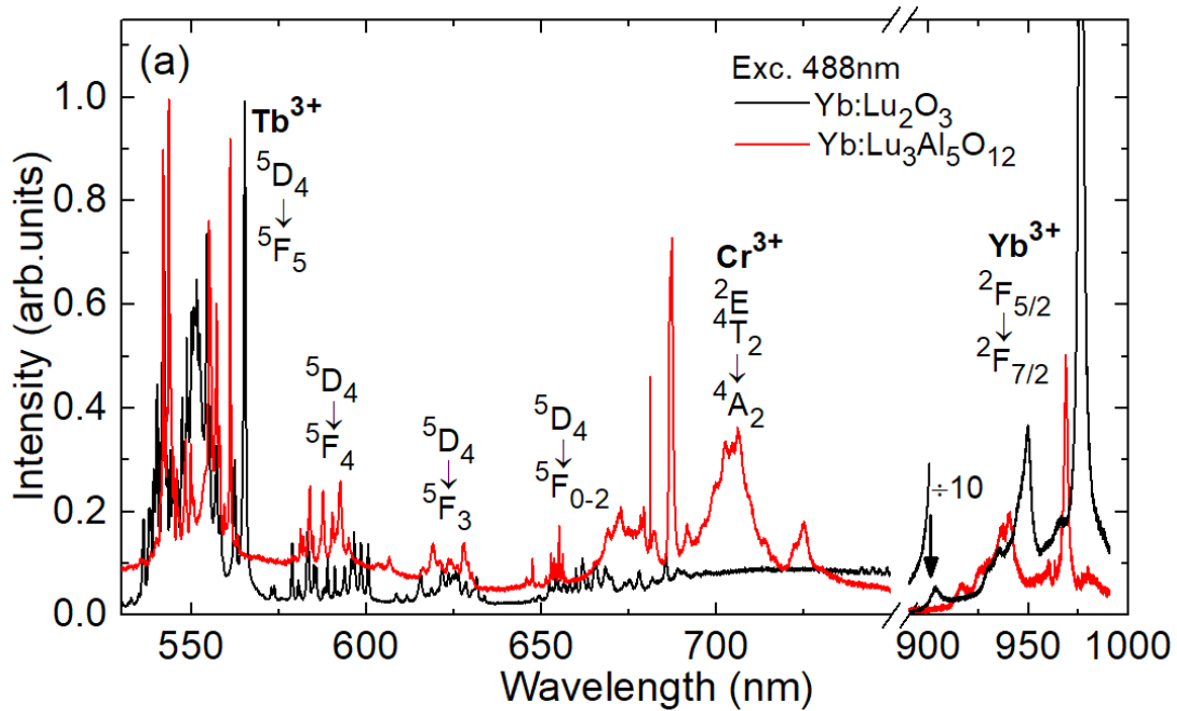


Table 1. Output characteristics^a of Yb:Lu₃Al₅O₁₂ crystalline and ceramic lasers.

Material	Doping, at.%	λ_P , nm	P_{th} , W	P_{out} , W	η , %	λ_L , nm	Ref.
Crystal	12	970	0.75	0.17 ^{CW}	~15	1078	[24]
Crystal	5	940	0.15	1.63 ^{CW}	72	1030	[42]
Crystal	10	968	0.5	3.0 ^{CW}	35	1048	[43]
		936	0.5	11.8 ^{qCW}	82	1046	[43]
Ceramics	3.6	968	0.45	5.65 ^{CW}	67.2	1031	^b
		968	0.45	8.83 ^{qCW}	66.9	1031	^b
Ceramics	5.0	~980	~0.9	7.2 ^{CW}	65	1030	[23]
Ceramics	10	940	0.47	2.14 ^{CW}	72	1032, 1047	[18]
Ceramics	10	936	~0.5	6.0 ^{CW}	52	1030	[25]
		936	-	8.83 ^{qCW}	60.2	1030	[25]

^a P_{th} – laser threshold, P_{out} – output power, η – slope efficiency (vs. absorbed pump power), λ_P – pump wavelength, λ_L – laser wavelength. ^bThis work.